New insights into SMOS sea surface salinity retrievals in the Arctic Ocean

Alexandre Supply, Jacqueline Boutin, Jean-Luc Vergely, Nicolas N. Kolodziejczyk, Gilles Reverdin, Nicolas Reul, Anastasiia Tarasenko

New insights into SMOS Sea Surface Salinity retrievals in the Arctic Ocean.

Alexandre Supply[1], Jacqueline Boutin[1], Jean-Luc Vergely[2], Nicolas Kolodziejczyk[3], Gilles Reverdin[1], Nicolas Reul[3] and Anastasiia Tarasenko[3,4].

[1]LOCEAN-IPSL, Sorbonne Université-CNRS-IRD-MNHN, Paris, France

[2]ACRI-St, Guyancourt, France

[3]Laboratoire d'Océanographie Physique et Spatiale (LOPS), Univ. Brest, CNRS, Ifremer, IRD, Brest, France

[4]Arctic and Antarctic Research Institute, Saint-Petersburg, Russia

Abstract

Since 2010, the Soil Moisture and Ocean Salinity (SMOS) satellite mission monitors the earth emission at L-Band. It provides the longest time series of Sea Surface Salinity (SSS) from space over the global ocean. However, the SSS retrieval at high latitudes is a challenge because of the low sensitivity L-Band radiometric measurements to SSS in cold waters and to the contamination of SMOS measurements by the vicinity of continents, of sea ice and of Radio Frequency Interferences. In this paper, we assess the quality of weekly SSS fields derived from swath-ordered instantaneous SMOS SSS (so called Level 2) distributed by the European Space Agency. These products are filtered according to new criteria. We use the pseudo-dielectric constant retrieved from SMOS brightness temperatures to filter SSS pixels polluted by sea ice. We identify that the dielectric constant model and the sea surface temperature auxiliary parameter used as prior information in the SMOS SSS retrieval induce significant systematic errors at low temperatures. We propose a novel empirical correction to mitigate those sources of errors at high latitudes.

Comparisons with in-situ measurements ranging from 1 to 11 m depths spotlight huge vertical stratification in fresh regions. This emphasizes the need to consider in-situ salinity as close as possible to the sea surface when validating L-band radiometric SSS which are representative of the first top centimeter.

SSS Standard deviation of differences (STDD) between weekly SMOS SSS and in-situ near surface salinity significantly decrease after applying the SSS correction, from 1.46 pss to 1.28 pss. The correlation between new SMOS SSS and in-situ near surface salinity reaches 0.94. SMOS estimates better capture SSS variability in the Arctic Ocean in comparison to TOPAZ reanalysis (STDD between TOPAZ and in-situ SSS = 1.86 pss), particularly in river plumes with very large SSS spatial gradients.

1. Introduction

In the context of global warming, Arctic is experiencing an increase of temperature two to three times higher than the global mean average (IPCC, 2018). The freshwater cycle in that region is profoundly modified. The salinity is decreasing (see a review in Carmack et al., 2016) except in the Barents Sea where both temperature and salinity are increasing under the effect of 'Atlantification', i.e. increase of salty supply from North Atlantic waters (Lind et al., 2018). Eventually, in the Arctic Ocean, salinity is the key dynamical variable, ensuring the stability of the water column and controlling the ocean circulation (Carmack., 2007).

The high variability of freshwater inputs is a dominant feature of the Arctic Ocean and induces a large variability in salinity (Carmack et al., 2015; Haine et al., 2015). In addition to the seasonal freshwater input from ice melting, the Arctic Ocean sea surface salinity (SSS) is mainly controlled by numerous river inputs. The Arctic Ocean covers only 1.2% of the global ocean but collects 11% of the freshwater from global river plumes (Shiklomanov et al., 1998) mainly in the interior shelves of the Kara, Laptev and East-Siberian Seas. In addition, the surface water entering poleward through Bering Strait is rather fresh in comparison with salty

50 waters from Atlantic. The third major net source of freshwater in the Arctic Ocean comes from
51 air-sea exchange (precipitation minus evaporation). Freshwater is exported equatorward from
52 the Arctic Ocean at Fram Strait, over the east Greenland shelves, as well as through Davis Strait
53 after crossing Baffin Bay.

54 Since 2010, L-Band radiometer satellite missions (SMOS (2010-present), Kerr et al., 2010,
55 Font et al., 2010), Aquarius (2011-2015, Lagerloef et al., 2013) and SMAP (2015-present,
56 Piepmeier et al., 2017) have demonstrated their abilities to monitor salinity variability at various
57 temporal and spatial scales in synergy with in-situ measurements as reviewed by Vinogradova
58 et al. (2019) and Reul et al. (2020). L-Band radiometry is of particular interest in the Arctic
59 Ocean as it combines the ability to retrieve thin sea ice thickness and salinity. SMOS is the first
60 satellite mission carrying an L-band radiometer (the MIRAS interferometer) allowing to
61 retrieve SSS with an unprecedented temporal coverage. It follows a sun-synchronous circular
62 orbit.

63 L-Band radiometer measurements are significantly less sensitive to SSS in cold water than
64 in warm tropical conditions (Meissner et al., 2016). However, a very large range of SSS is
65 observed in the Arctic, with salinity close to 0pss in river plumes and reaching 35 pss in the
66 Atlantic water (Carmack et al., 2015). For this reason, L-Band radiometry remains valuable for
67 the detection of large SSS variability and the monitoring of oceanic fronts in the Arctic Ocean
68 (Brucker et al. 2014; Matsuoka et al., 2016; Olmedo et al., 2018; Tang et al., 2018; Tarasenko
69 et al. 2019).

70 Brucker et al. (2014) and Tang et al (2018) presented capabilities (monitoring of the river
71 plumes and of upper layer freshwater exchanges between different Arctic Seas and sub-Arctic
72 Oceans) and limits (sea-ice presence) of L-Band SSS retrievals based on Aquarius and SMAP
73 measurements respectively. Köhler et al. (2015) found sea surface temperature (SST) - related
74 bias (-1.2 pss) of SMOS SSS retrieved in cold waters and pollution due to Radio Frequency

Interference (RFI) in the northern North Atlantic. Matsuoka et al. (2016) used SMOS SSS monitoring together with ocean color remote sensing in order to detect the origin (river or ice melting) of salinity interannual anomalies close to the Mackenzie river mouth. Tarasenko et al. (2019) showed the atmospheric influence on the river plume variability in the Laptev Sea at intra-seasonal time scale (a few weeks) based on SMOS SSS. Recently, an SSS retrieval methodology alternative to the one in place in the ESA L2 chain has been proposed with new systematic bias corrections and filtering adjusted to the Arctic Ocean conditions (Olmedo et al., 2018).

Using an accurate SST is critical in order to retrieve SSS with a minimum uncertainty. For instance, at SST=5 °C and SSS=35 pss, an error of 1°C roughly leads to an error of 0.1 K in brightness temperature (TB), which translates into in error of 0.3 pss in the retrieved SSS (Yueh et al., 2001). According to Stroh et al (2015) and Høyer et al (2012), systematic differences of various space-based SST measurements in the Arctic Ocean, estimated by comparisons with buoys and ship-based measurements, range from 0.3 to 0.5 °C depending on the season and on the sensor. The temporal and spatial resolution of the SST fields obtained by different optimal analyses vary significantly. This results in significant differences in the estimated SST over highly dynamical and variable regions such as river plumes. A satellite SSS bias related to SST may also be due to flaws in the dielectric constant model that links TB to SSS and SST (Dinnat et al., 2019). The presence of badly detected sea ice can also lead to negative bias on the retrieved SSS (Tang et al., 2018).

The satellite SSS validation is made difficult because of the strong vertical haline stratification observed in the upper Arctic Ocean waters, as L-band radiometer only senses the top centimeter of the ocean (Boutin et al., 2016) and most in-situ sensors probe salinity much deeper (meters). This stratification varies geographically and temporally. The depth of the

mixed layer (ML) may be shallower than 10 m in summer in some regions such as the Beaufort Sea (Peralta-Ferriz et al., 2015).

This paper focuses on validating weekly fields derived from the European Space Agency (ESA) SMOS level 2 (L2) SSS, analyzing potential sources of errors and proposing improvements. A description of the data and methods is first given (section 2 and 3). The influence of stratification on the SSS validation is then investigated (section 4). A first correction of SSS is derived using the pseudo dielectric constant parameter retrieved by the SMOS ESA L2 processing (Waldteufel et al., 2004). The influence of the prior SST on SSS retrieval is further analyzed (section 5). Finally, corrected SMOS weekly SSS are compared against surface salinity from TOPAZ reanalysis and in situ measurements from vessels transect to assess the product content from short to interannual time scales (section 6).

2. Data

2.1. Satellite related parameters

2.1.1. SST

In the SMOS L2 SSS processor, SST provided by European Centre for Medium-Range Weather Forecasts (ECMWF) Integrated Forecasting System (SST_{ECMWF}) are used as priors in the SSS retrievals. These forecasts are initialized 6 to 12 hours before by OSTIA SST (Donlon et al., 2012; ECMWF, 2016). The OSTIA SST analysis is generated using a multiscale interpolation of various satellite SST (infrared and microwave SST) and in-situ measurements at a grid spacing close to 5km.

In this paper, we compare SST_{ECMWF} with the 9 km grid resolution infrared and microwave OI SST produced by REMSS (SST_{REMSS}) that relies on an optimal interpolation of infrared and microwave measurements, but no in-situ measurements

(http://www.remss.com/measurements/sea-surface-temperature/oisst-description/). The influence of the SST differences onto the retrieved SSS is estimated as described in section 5.3.

2.1.2. SMOS L2 SSS and Acard

We use the SMOS L2 SSS (uncorrected for Land Sea Contamination) v662 distributed by ESA from 2011 to 2017 in the region bounded by latitude 60°N and 90°N. These products are organized in ½ orbits of instantaneous SSS retrievals. The principle of the ESA L2 SMOS SSS retrieval is recalled in (Boutin et al., 2018; section 3.1 and documents cited herein). SSS are oversampled over an Icosahedral Snyder Equal Area (ISEA) grid at 15 km resolution but the mean spatial resolution of ESA L2 SMOS SSS is close to 50 km. The dielectric constant model of sea water used in the SMOS processor is the Klein and Swift (1977) model (hereafter KS).

We also use the pseudo dielectric constant (Acard) parameter. Acard is an effective L-band dielectric constant retrieved from ~hundreds SMOS multi-angular TB, independent of any SSS or dielectric constant model assumption. It was designed to integrate all available information about surface dielectric characteristics (Waldteufel et al. 2004). Acard allows to synthesize in one parameter the information on the dielectric constant that is contained in all SMOS TB. Since the noise on individual TB is large (2-3 K), Acard synthesis allows a more precise filtering than a filtering applied on each individual TB. SMOS SSS and Acard are retrieved using a Bayesian approach through the minimization of the χ^2 cost function:

$$\chi^2 = \sum_{n=1}^{N} \frac{[Tb_n^{meas} - Tb_n^{mod}(\theta_n, P_i \ldots)]^2}{\sigma_{Tbn}^2} + \sum_{n=1}^{M} \frac{[P_i - P_{io}]^2}{\sigma_{Pio}^2} \qquad (1)$$

where N is the number of measurements available for retrievals in vertical and horizontal polarizations at different incidence angles θ_n, P_i are prior parameters, Tb^{meas} are measured TB corrected for some phenomena, Tb^{mod} are modelled TB. These various components are described for each retrieval in Table 1. Retrievals are initialized with European Centre for Medium-Range Weather Forecasts (ECMWF) (wind speed (WS_{ECMWF}), SST

148 (SST_{ECMWF})). In case of SSS retrieval, both wind speed (WS_{L2}) and SST (SST_{L2}) are retrieved
149 together with SMOS SSS (SSS_{L2}). In case of Acard retrieval ($Acard_{L2}$) only SST (SST_{ACARD})
150 is retrieved together with Acard. A detailed description of the Acard retrieval in the L2 Ocean
151 Salinity processor is given in appendix-A.

152 Acard as simulated with KS sea water dielectric constant and ice dielectric constant
153 reported in (Ulaby, 1990), varies from approximately 50 in pixels totally covered with sea water
154 to a value close to 0 in pixels totally covered by ice. Hence, pixels partially covered by sea ice
155 exhibit lower Acard values than pure water pixels.

156 Table 1: Summary of SMOS SSS and Acard retrieval principle in the SMOS L2OS processor.

	SSS retrieval	**Acard retrieval**
Modeled TBs	Dielectric constant, wind, galactic, atmospheric model components	Flat sea emission
Measured TBs	SMOS multi-angular TBs	SMOS multi-angular TBs corrected from wind, galactic and atmospheric model components
Prior variables	WS_{ECMWF}, SST_{ECMWF}	SST_{ECMWF}
Retrieved variables	SSS_{L2}, WS_{L2}, SST_{L2}	$Acard_{L2}$, SST_{Acard}

157

158 2.1.3. Pre-processed SMOS L3 maps

159 Level 3 (L3) 7-day moving averages of SMOS ESA L2 parameters are produced each
160 day. The 15-km ISEA grid is kept from L2 to L3, in order to avoid spatial smoothing. Only
161 pixels further than 40 km from land are considered. Each SSS or Acard entering the 7-day
162 average is weighted by a Gaussian weight function with a 3-day standard deviation and by the
163 L2 uncertainty taken as the L2 SSS theoretical error multiplied by the χ^2 value (L2 SSS error
164 and χ^2 estimates are described in Boutin et al., 2018). Level 2 products' flags raised for strong
165 sunglint ('Dg_sun_glint_fov'), moonglint ('Dg_moonglint'), or galactic glints
166 ('Dg_galactic_Noise_Error') are filtered out. L2 measurements for which WS_{ECMWF} is lower
167 than 3 $m.s^{-1}$ or greater than 12 $m.s^{-1}$ are not considered due to larger uncertainties with the
168 roughness model for these ranges of wind speed. L3 SSS uncertainty is estimated through an
169 error propagation of L2 SSS uncertainty estimates.

170 Frequent revisit of polar areas by SMOS allows typically between 0 and 50 L2 retrievals in
171 each pixel within 7 days. We remove L3 pixels with less than five L2 retrievals and with an
172 average distance to the center of the SMOS track higher than 200km in order to minimize the
173 influence of uncertain measurements at the edge of the swath. We name SSS_{SMOS} the SMOS
174 SSS obtained after this processing.

175 2.2. Model reanalysis

176 We use ARCTIC_REANALYSIS_PHYS_002_003 distributed by the Copernicus Marine
177 Environment Monitoring Service (CMEMS). This product is based on the TOPAZ system in
178 its version 4 (Sakov et al., 2012) that uses the HYCOM model (Chassignet et al., 2009). The
179 TOPAZ reanalysis ingests various in-situ and satellite measurements in order to provide fields
180 of temperature, salinity, sea ice drift or sea ice concentration. Salinity measured by Argo floats
181 and some research cruises are assimilated. TOPAZ does not assimilate SMOS SSS.

182 The initialization of the model is performed in 1973 with a combination of World Ocean
183 Atlas climatology (WOA05) and Polar Science Center Hydrographic Climatology (PHC
184 version 3.0). In addition to the initialization, a climatology of river runoff is used in order to
185 resolve remaining inaccuracies in evaporation and run-off (CMEMS Arctic Ocean Physical
186 Reanalysis Product User Manual). The river discharge monthly climatology is derived using
187 the Total Runoff Integrating Pathways (TRIP, Oki and Sud., 1998) and run-offs estimates from
188 ERA-interim. SMOS SSS are compared with TOPAZ surface salinity simulated at 0m depth
189 (SSS_{TOPAZ}). We also used Sea Ice Concentration (SIC) from TOPAZ reanalysis in order to study
190 the influence of sea ice on SMOS SSS.

191 2.3. In-situ measurements

192 Satellite L3 parameters are collocated with in situ measurements described below using a
193 nearest neighbor criteria.

194 2.3.1. Argo profilers

195 Salinity and temperature from Argo profiling floats are taken from the Coriolis GDAC
196 (Global Data Argo Center, http: //www.coriolis.eu.org/). Only measurements flagged as good
197 (flag 1), between 1 and 10 m depth are used.

198 Argo floats are mainly located in the North Atlantic Ocean between 60°W and 20°E
199 (Figure 1A), with a few floats in the Chukchi Sea. This spatial distribution results in a very
200 peaky salinity distribution, with a salinity mode close to 35 pss and very few salinities below
201 34pss (Figure 1D).

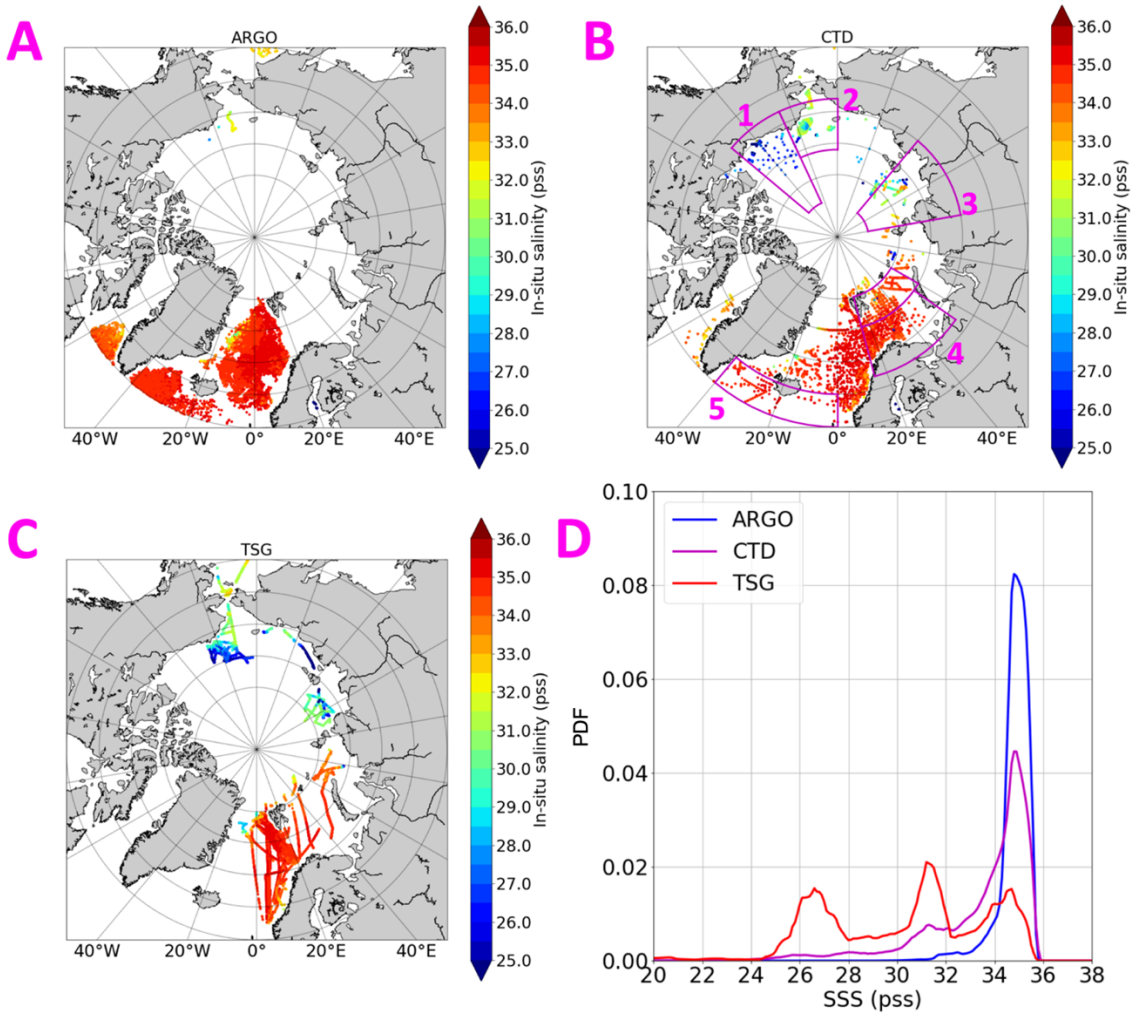

Figure 1: In-Situ near-surface salinity measured at the location of (A) Argo floats (B) CTD casts in different study areas (1 - Beaufort Sea, 2 - Chukchi Sea, 3 - Laptev Sea, 4 - Barents Sea, 5 – Atlantic area) and (C) underway TSG. (D) Probability density function (PDF) of salinity observed with the different devices.

2.3.2. CTD profiles

A large part of the CTD profiles is downloaded from the Coriolis data center. We also consider CTD profiles:

- from two NABOS cruises, in 2013 (Ivanov et al., 2013) and 2015 (Polyakov et al., 2015), in the Kara Sea, Laptev Sea and East-Siberian Sea;

- from the Arctic Floating University collected in 2012 (Makhotin and Ivanov, 2018a), 2013 (Makhotin and Ivanov, 2018b) and 2014 (Makhotin and Ivanov, 2018c) in the Barents Sea,
- collected in the Laptev Sea and East-Siberian Sea during Swerus C-3 cruise (Björk, 2017);
- in the Beaufort Sea from the Beaufort Gyre Exploration Project website (https://www.whoi.edu/website/beaufortgyre/home).

Only measurements between 1 and 10 m are considered. We noticed a few CTD erroneous measurements. In order to ensure that suspicious measurements are not considered in the validation, we apply a 3σ-filtering with respect to SSS_{TOPAZ} (see section 2.3; only in-situ measurements with an absolute difference between $S_{in\text{-}situ}$ and SSS_{TOPAZ} lower than 3σ (5.85pss) are kept).

CTD casts in the Arctic Ocean cover a larger range of temperature and salinity than Argo (Figure 1B, 1D). Indeed, the CTD dataset samples very low salinity areas in the Arctic Ocean in the Beaufort gyre or river plumes, as for example in the Laptev Sea or East-Siberian Sea.

2.3.3. Underway thermosalinographs (TSG)

Underway TSG data used in this study are recorded by 4 different vessels: the R/V Heincke, the R/V Polarstern, the R/V Mirai and the S/V Tara. Data of R/V Heincke and R/V Polarstern are downloaded on PANGAEA website (https://www.pangaea.de) and listed in the Appendix-B. R/V Mirai data of the year 2012 (JAMSTEC, 2015a), 2013 (JAMSTEC, 2015b) and 2014 (JAMSTEC, 2018) are downloaded on the DARWIN website of JAMSTEC (http://www.godac.jamstec.go.jp/darwin/e). S/V Tara measurements, that were quality checked at LOCEAN, are available on the Coriolis website. TSG measurements are taken at different depths, from 1m on S/V Tara to 11m for R/V Polarstern.

233 Underway TSGs salinities are the most variable (Figure 1C). Their statistical distribution is
234 characterized by three modes, a first mode is between 34 and 36 pss, a second mode between
235 31 and 32 pss and, finally, a third mode between 25 and 27 pss. Underway TSGs have a similar
236 geographical sampling as CTD casts but with more measurements closer to coast and a better
237 sampling of river plumes.
238
239 3. Influence of salinity vertical stratification on satellite/in-situ comparisons
240 3.1. Depth dependency: case of CTD profiles
241 We analyzed the effect of stratification on the differences between in-situ salinity (S_{insitu})
242 and SSS_{SMOS}. Figure 2 presents the effect of stratification on mean comparisons between S_{insitu}
243 and SSS_{SMOS} considering different depths. We consider here only CTD casts which provide the
244 most complete depth and spatial coverage in the studied areas. Two cases are examined : cases
245 with a difference lower than -0.1 pss between shallower (salinity average from 1m to 5m) and
246 deeper levels (salinity average from 5m to 10m) named "stratified" cases ($\overline{S_{insitu[0m:5m]}} -$
247 $\overline{S_{insitu[5m:10m]}} < -0.1\ pss$) and cases with a difference higher than -0.1 pss between shallower
248 (salinity average from 1m to 5m) named "no-stratified" cases ($\overline{S_{insitu[0m:5m]}} -$
249 $\overline{S_{insitu[5m:10m]}} > -0.1\ pss$). The -0.1 pss threshold is chosen arbitrary in a context of SSS
250 validation. For "stratified cases", we observe a continuously increasing difference between
251 S_{insitu} and SSS_{SMOS} with depth. In the "no-stratified" cases, as expected the difference is stable
252 as a function of depth, but a slight difference remains between 1m and 2m depth (Figure2A).
253 Stratified cases are mainly recorded over shelf seas and in river plumes areas (Figure 2B). Cases
254 without stratification are mainly recorded in the North Atlantic and Barents Sea. Considering
255 3228 CTD profiles: 81% are considered as not stratified whereas 19% are considered as
256 stratified (Figure 2C). Comparison of SSS_{SMOS} with S_{insitu} at all depths show a higher scatter for
257 "no-stratified" cases than for stratified cases (Figure 2D).

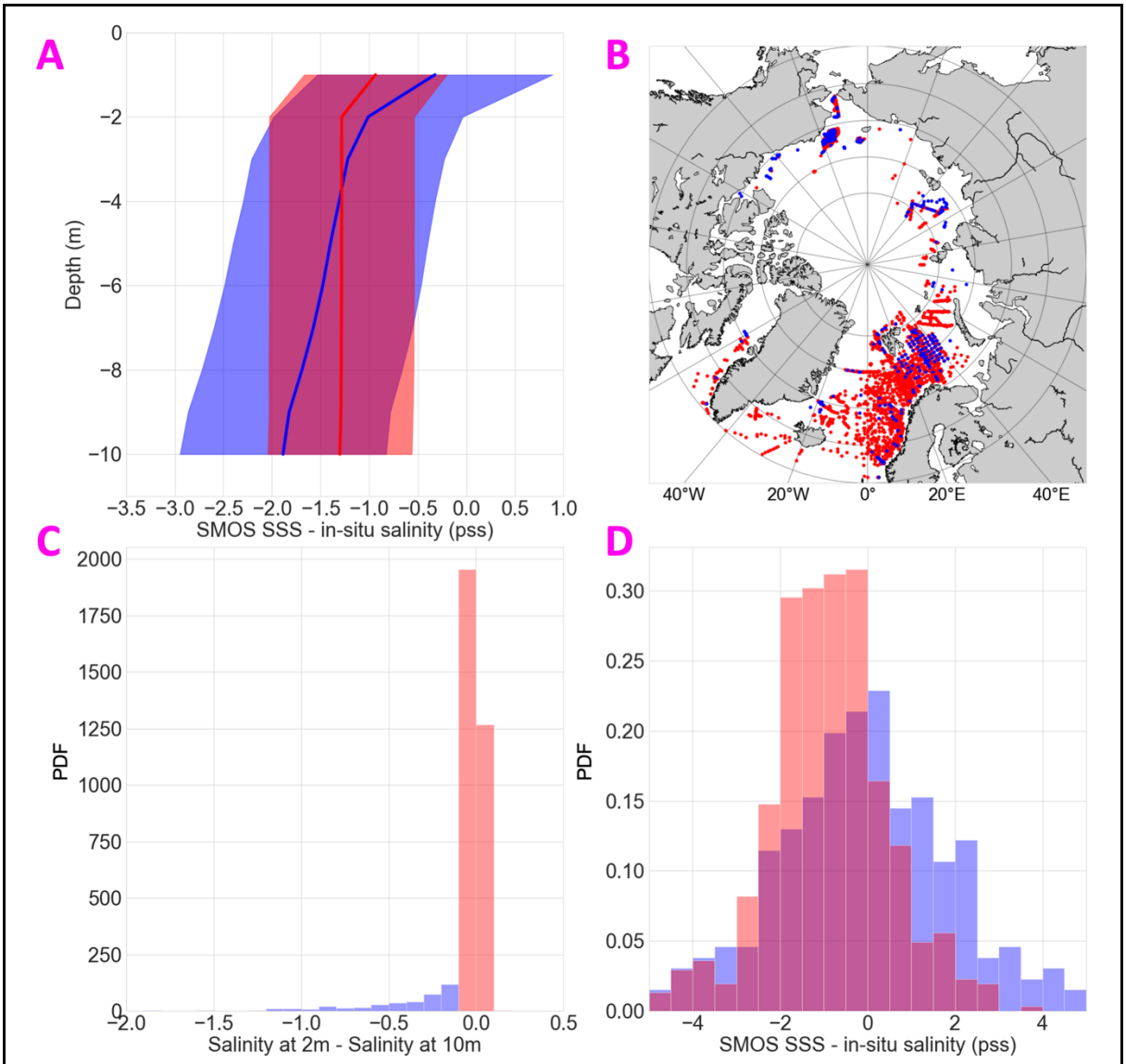

Figure 2: (A) Averaged differences between S_{insitu} and SSS_{SMOS} as a function of depth in stratified and not-stratified cases (shaded area represents 2 × standard deviation) ; (B) Geographical distribution of stratified and not stratified cases; (C) Statistical distribution of differences between shallower (salinity average from 1m to 5m) and deeper levels (salinity average from 5m to 10m) for different CTD profiles; (D) Statistical distribution of differences between SSS_{SMOS} and in-situ salinity for stratified and not-stratified cases. "Stratified cases" ($\overline{S_{insitu[0m:5m]}} - \overline{S_{insitu[5m:10m]}} < -0.1\ pss$) are in blue and "not-stratified" cases ($\overline{S_{insitu[0m:5m]}} - \overline{S_{insitu[5m:10m]}} > -0.1\ pss$) are in red.

258

3.2. Study areas

In the present study, we focus our investigations on five study areas representing two inflow shelves with low stratification (Barents and Chukchi shelves), two more-stratified interior shelves (Laptev and Beaufort shelves) and an Atlantic area. The details are as follows:

- Beaufort Sea: between 155°W and 130°W and between 68°N and 84°N; the Beaufort Sea is characterized by the presence of the Beaufort gyre and a river plume from the Mackenzie river; the collocation dataset records the lower salinity values in the Beaufort Sea;
- Chukchi Sea: between 68°N and 76°N and between 155°W and 180°W; the Chukchi Sea is a shallow sea dominated by a freshwater inflow from the Pacific Ocean;
- Laptev Sea: between 100°E and 140°E; the Laptev Sea is influenced by freshwater from the Lena river plume, an inflow of freshwater from the Kara Sea, and salty water from the Atlantic Ocean above the continental slope;
- Barents Sea: between 75° and 80° N and between 15°E and 60°E; and between 60°E and 67°N and between15°E and 55°E; the Barents Sea is dominated by inflow from the Atlantic characterized by salty waters with respect to other study areas. The SSS variability of this area is less pronounced than in the previous areas.
- Atlantic area: between 60°N and 65°N and between 40°W and 0°W; this area represents the highest SSS of the study and the lowest variability of the SSS.

The depth of the in-situ measurement plays a different role in different areas. Figures 3 and 4 compare CTD measurements with SSS_{SMOS} for each study area. In the salty regions (Barents Sea and Atlantic area, Figure 3), the depth of in-situ measurements does not seem to influence strongly the relationship between S_{insitu} and SSS_{SMOS}. These areas demonstrate very stable mean (MoD) and STD (STDD) difference between S_{insitu} and SSS_{SMOS}.

283 In fresher regions (Figure 5), in the Beaufort and Laptev Sea (figures 4A, B and 4E, F),
284 where the runoff of the Mackenzie and the Lena river are observed, important differences
285 between SSS_{SMOS} and in-situ measurements are observed when the depth of the in-situ
286 measurement increases. In the Laptev Sea, it is even stronger when the surface salinity is lower,
287 indicating a stronger stratification. In the Chukchi Sea (Figure 4C, D), the stratification effect
288 is less pronounced than in the Beaufort and the Laptev Seas. Figures 3 and 4 clearly show that,
289 as expected, stratification increases when the observed surface salinity decreases. In the
290 Beaufort Sea, the average difference between 1 m and 10 m depth is -1.84 pss (Figure 4B). In
291 the Laptev Sea, average difference between 2 m and 10 m depth is -1.47 pss (Figure 4F). The
292 STDD between SSS_{SMOS} and S_{insitu} is also strongly affected by the stratification: in the Beaufort
293 Sea STDD increase from 1.47 pss (1 m depth) to 2.29 pss (10 m depth) and from 1.83 pss (2 m
294 depth) to 2.12 pss (10 m depth) in the Laptev Sea.

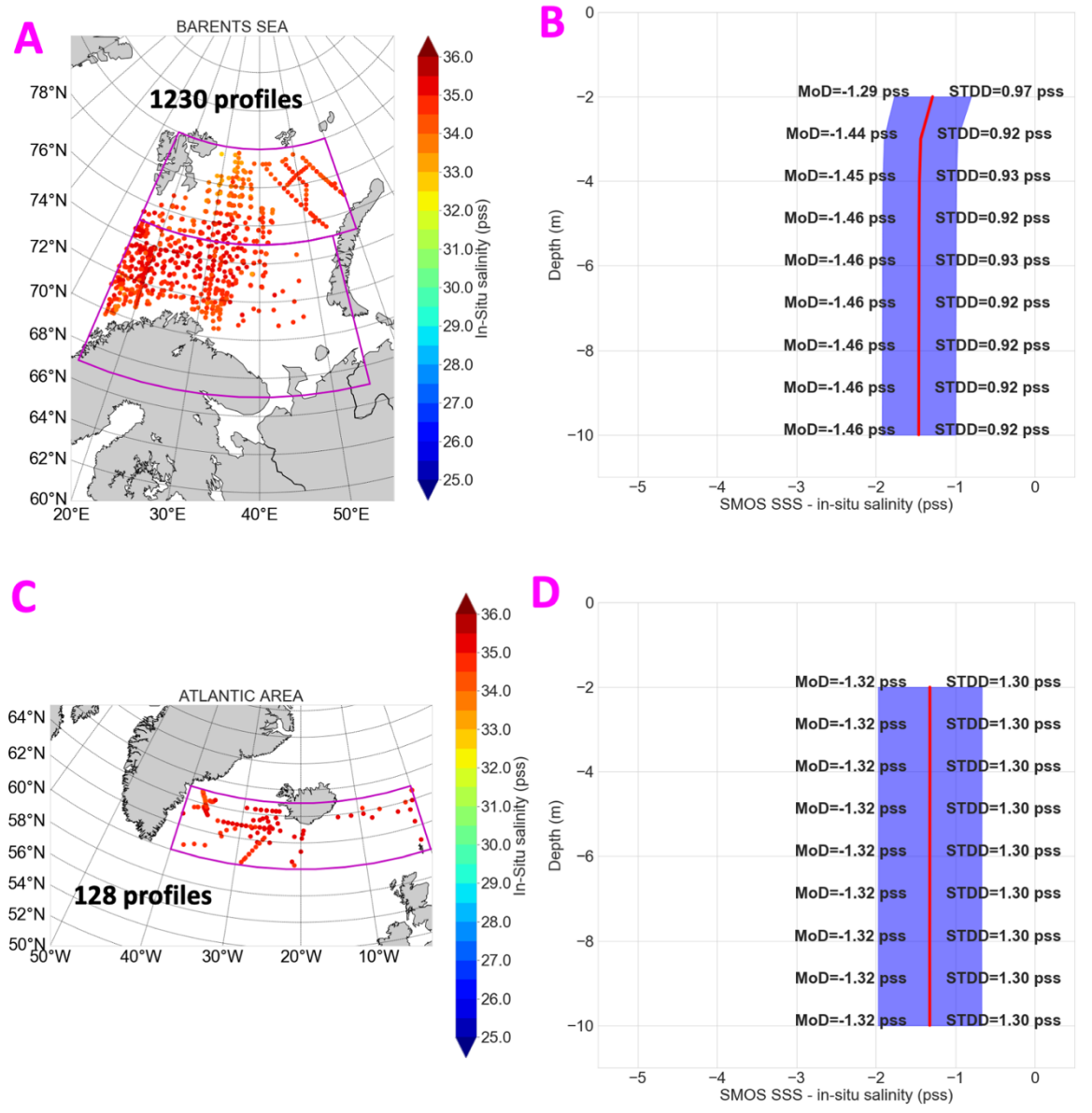

Figure 3: Effect of stratification on relationship between SSS_{SMOS} and in-situ salinity measurements in salty regions : (A, C) coordinates of colocalizations between SMOS and CTD profiles in different study areas (Barents Sea, Atlantic area); (B, D) MoD between SSS_{SMOS} and in-situ salinity for different depths (from CTD casts only, with shaded area representing 2 standard deviation).

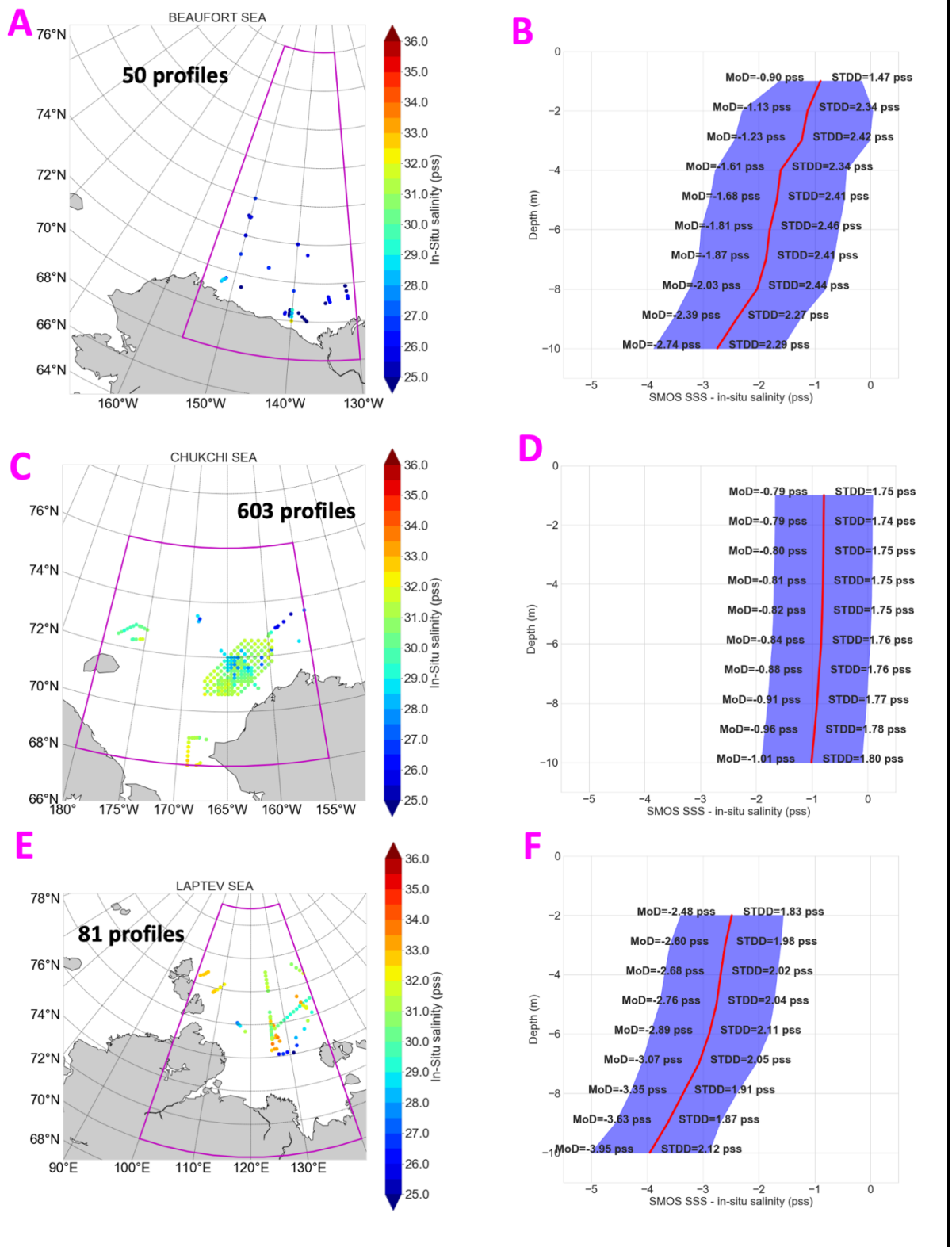

Figure 4: Effect of stratification on the relationship between SSS_{SMOS} and in-situ salinity measurements in fresh regions : (A, C, E) coordinates of colocalizations between SMOS and

CTD profiles in the different study areas (Beaufort Sea, Chukchi Sea, Laptev Sea); (B, D, F) MoD between SSS_{SMOS} and in-situ salinity for different depths (from CTD casts only, with shaded area representing 2 standard deviation).

295

296 3.3. Selection of in-situ measurements for absolute SSS calibration and validation

297 The selection of S_{insitu} for comparison and validation with satellite SSS is a compromise
298 between the need for a set of in-situ measurements representative of the whole Artic Ocean and
299 the need for in-situ measurements representative of SMOS estimates (1cm depth).

300 We select S_{insitu} according to depth in order to avoid as much as possible the effect of vertical
301 stratification. However, in situ measurements between 1m and 5m depth cover much broader
302 regions and in particular fresh areas not sampled by in situ measurements between 1m and 3m
303 depth (Appendix-C). Hence, for the validation purpose (section 5.2), the maximum depth of
304 S_{insitu} is set at 5m.

305 On the other hand, the absolute calibration (constant bias removal) of SMOS SSS is
306 performed in a salty area less prone to stratification effects, the Barents Sea, where we only
307 consider the uppermost S_{insitu}.

308

309 4. Novel corrections and filtering: methodology

310 4.1. Sea ice and outliers filtering: Acard

311 A main contamination of satellite SSS at high latitude comes from the presence of sea ice
312 (Tang et al. 2018) which emissivity is much higher than the one of the surface ocean due to a
313 much lower dielectric constant. Our filtering procedure will take advantage of L3 Acard.

314 Acard may be retrieved directly from SMOS TB and a prior SST, considering only
315 emissivity and Fresnel equations, independently from the dielectric constant model (Table 1).
316 It is named $Acard_{SMOS}$ below. It is also possible to compute Acard ($Acard_{KS}$) from a theoretical

dielectric constant model using equation [A2] (Appendix-A). We use the KS dielectric constant model also used to retrieve SSS in the L2 OS processor. The difference between $Acard_{SMOS}$ and $Acard_{KS\ (SMOS\ SSS,\ ECMWF\ SST)}$ (D_{Acard}=$Acard_{SMOS}$ − $Acard_{KS\ (SMOS\ SSS,\ ECMWF\ SST)}$) may result from either:

- an imperfect representation of the dielectric properties of the observed surface by the KS model, or,
- uncertainties on the SSS and SST priors used to compute $Acard_{KS}$, or,
- residual errors in the correction of atmospheric, solar and sky glint, or sea surface roughness used to estimate the flat sea surface radio-brightness contrast, or,
- And/or from corrupted SMOS TB (RFI, image reconstruction errors, etc.) used to retrieved $Acard_{SMOS}$.

In the following, we address uncertainties coming from the first two items. We compute $Acard_{KS}$ using retrieved SMOS SSS and ECMWF SST ($Acard_{KS\ (SMOS\ SSS,\ ECMWF\ SST)}$). Figure 5A illustrates the relationship between SSS and Acard for different SST. Academic simulations (not shown) suggest that $Acard_{SMOS}$ is much lower than $Acard_{KS\ (SMOS\ SSS,\ ECMWF\ SST)}$ when sea ice is present within a SMOS pixel.

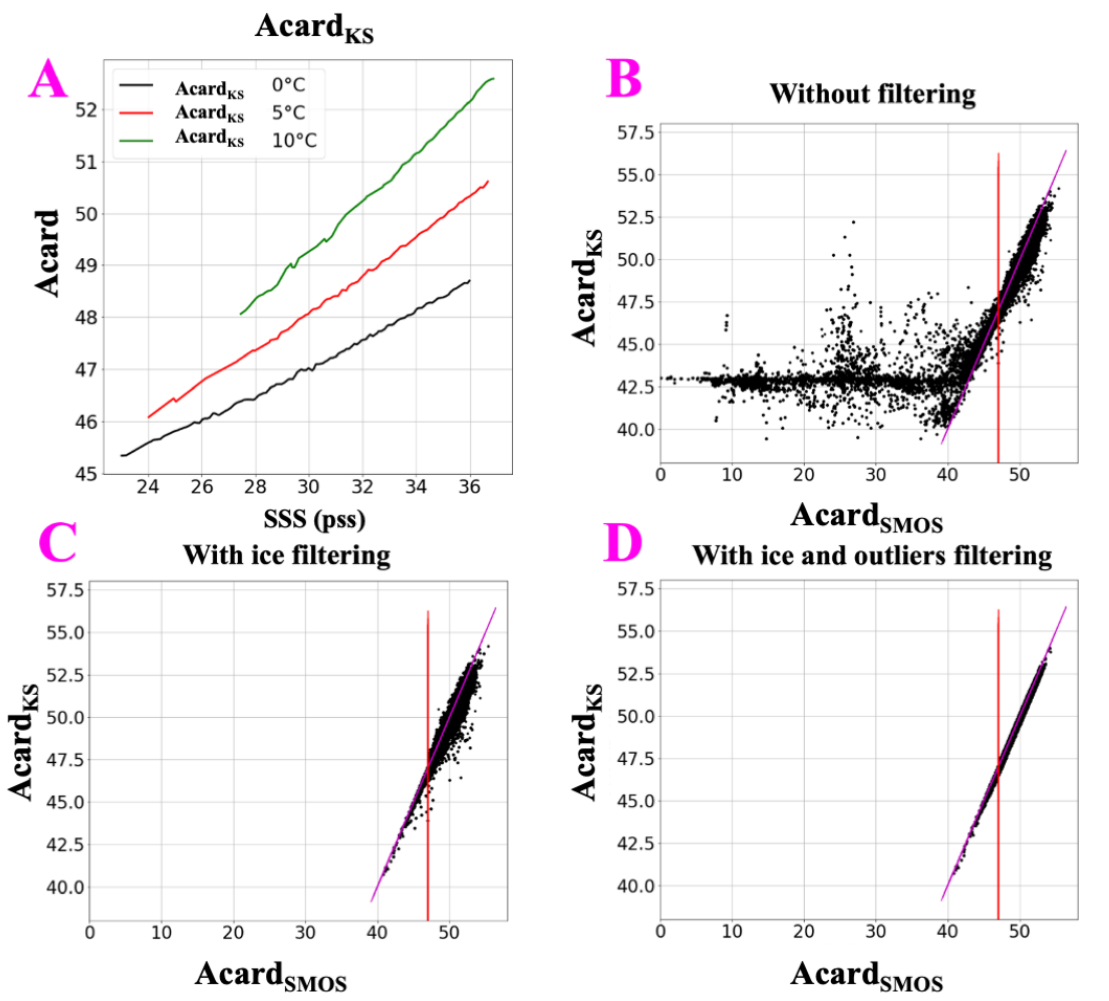

Figure 5: (A) Relationship between Acard and SSS at various SST considering KS model; (B) Scatterplot of $Acard_{KS}$ versus $Acard_{SMOS}$ without filtering; (C) same as (B) with ice filtering (first step); (D) same as (B) with ice filtering and outliers filtering (second step); (red) $Acard_{SMOS}$ = 47 threshold; (magenta) line corresponding to $Acard_{KS}$ = $Acard_{SMOS}$.

Based on these considerations, we developed a two-step filtering methodology. As illustrated in Figure 5B which represents $Acard_{SMOS}$ as a function of $Acard_{KS\ (SMOS\ SSS,\ ECMWF\ SST)}$ without applying any filtering: two main regimes are observed. The first regime (points on the diagonal, above 40, Figure 5B), corresponds to the expected behavior between $Acard_{SMOS}$ and $Acard_{KS\ (SMOS\ SSS,\ ECMWF\ SST)}$ in the absence of sea ice. The second regime (plateau in

339 $Acard_{KS}$, below 40, Figure 5B) with large differences between $Acard_{SMOS}$ and $Acard_{KS\ (SMOS\ SSS,}$
340 $_{ECMWF\ SST)}$ is due to pixel partially covered by sea ice and/or an inappropriate use of KS in order
341 to compute Acard in these cases (KS model is designed for sea ice free ocean conditions). We
342 note that the probability to observe the second regime case strongly increases with an Acard
343 value lower than 47. In a first step, when Acard is less than 47, we apply a very restrictive filter
344 by removing all pixels with a D_{Acard} value lower than -0.1 (Figure 5C). In a second step, we
345 filter out D_{Acard} values lower than -0.21 and larger than 0.52, that correspond respectively to the
346 0.05 and 0.95 percentiles of D_{Acard} distribution after ice filtering (Figure 5D).

347 4.2. Absolute calibration of SSS

348 Considering differences with respect to upper S_{insitu} in the Barents Sea (Figure 3B), we add
349 1.29 pss to SMOS SSS for removing the SMOS SSS global bias.

350 4.3. Correction related to uncertainty on the dielectric constant model

351 Flaws in the dielectric constant model may lead to errors on both the retrieved SSS_{SMOS} and
352 SST_{SMOS} (as defined in Table 1) but not on $Acard_{SMOS}$ since the Acard retrieval is independent
353 of any dielectric constant model. As a first approximation, we assume that errors in the dielectric
354 model only induce biases in the retrieved SSS_{SMOS} and not on retrieved SST. We compare
355 $Acard_{SMOS}$ with $Acard_{KS}$ computed with parameters available in the SMOS User Data Product,
356 i.e. SSS_{SMOS} and SST_{ECMWF}. A first correction on SSS_{SMOS} can then be determined using the
357 following relationship that also consider absolute calibration (section 4.2.):

358 $$SSS_{SMOS\ A} = SSS_{SMOS} + \frac{(Acard_{KS} - Acard_{SMOS})}{\lambda(SST_{ECMWF}, SSS_{SMOS})} + 1.29 \qquad (2)$$

359 where $\lambda\ (SST, SSS) = \frac{\partial Acard_{KS}\ (SST,\ SSS)}{\partial SSS}$.

360 Figure 8 shows differences between $Acard_{SMOS}$ and $Acard_{KS}$. $Acard_{SMOS}$ is plotted as a
361 function of SST and $SSS_{SMOS\ A}$ - 1.29 in order to be comparable to $Acard_{KS}$ computed with
362 SSS_{SMOS} (Figure 6A). Differences between $Acard_{SMOS}$ and $Acard_{KS}$ are larger for low SSS and
363 low SST (Figure 6C). This correction integrates different biases that can not be disentangled in

this study: 1) SSS bias coming from the KS model; 2) SSS bias due to a potential difference between SST retrieved with SMOS and SST_{ECMWF}.

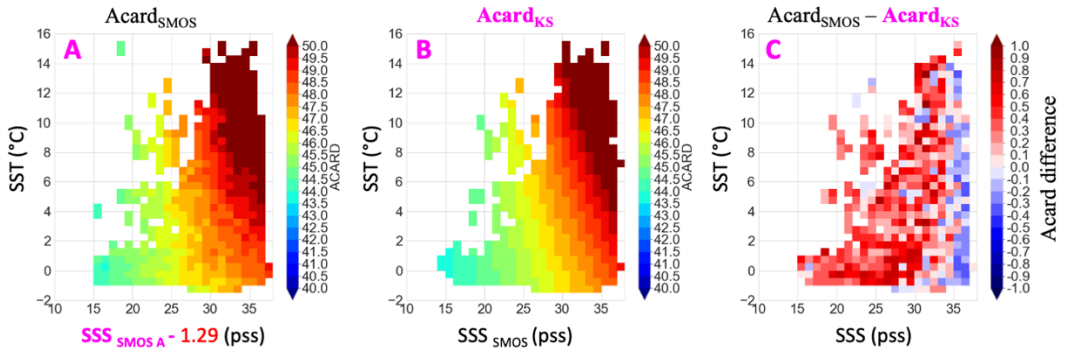

Figure 6: (A) $Acard_{SMOS}$ as a function of SST_{ECMWF} and $SSS_{SMOS\ A} - 1.29$ $Acard_{KS(SMOS\ SSS,ECMWF\ SST)}$; (B) $Acard_{KS(SMOS\ SSS,ECMWF\ SST)}$ as a function of SST_{ECMWF} and SSS_{SMOS}; (C) Difference between $Acard_{SMOS}$ and $Acard_{KS}$. SMOS retrieved variables are in black, computed variables are in magenta.

4.4. Correction linked to uncertainty on prior SST

We observe that in some regions such as the Lena river plume in the Laptev Sea, SST_{ECMWF} is nevertheless underestimated with respect to upper in-situ temperature, T_{insitu}. As shown in Appendix-D (Figure D1), stronger SST gradient are observed in REMSS SST product compared with OSTIA SST used in ECMWF. Based on the KS model, it is possible to compute a second correction of the retrieved SSS considering sensitivity to SST and selecting another SST product as reference (here chosen to be REMSS SST):

$$SSS_{SMOS\ A+T} = SSS_{SMOS\ A} + \frac{\gamma(SST_{ECMWF},SSS_{SMOS})}{\beta(SST_{ECMWF},SSS_{SMOS})}(SST_{ECMWF}\text{-}SST_{REMSS}) \quad (3)$$

where $\beta(SST, SSS) = \frac{\partial TB(SST,\ SSS)}{\partial SSS}$ and $\gamma(SST, SSS) = \frac{\partial TB(SST,\ SSS)}{\partial SST}$.

5. Results and validation

5.1. Validation of sea ice filtering

To assess the efficiency of the Acard filtering for sea ice we used SIC data from TOPAZ and we analyze a case study in the Laptev Sea. As illustrated on Figure 7, without the Acard filtering, low SSS values are observed in the northernmost areas in the vicinity of sea ice edges because of a too permissive filtering of ice in the ESA L2 processor. At these locations, negative D_{Acard} and positive SIC from TOPAZ are observed.

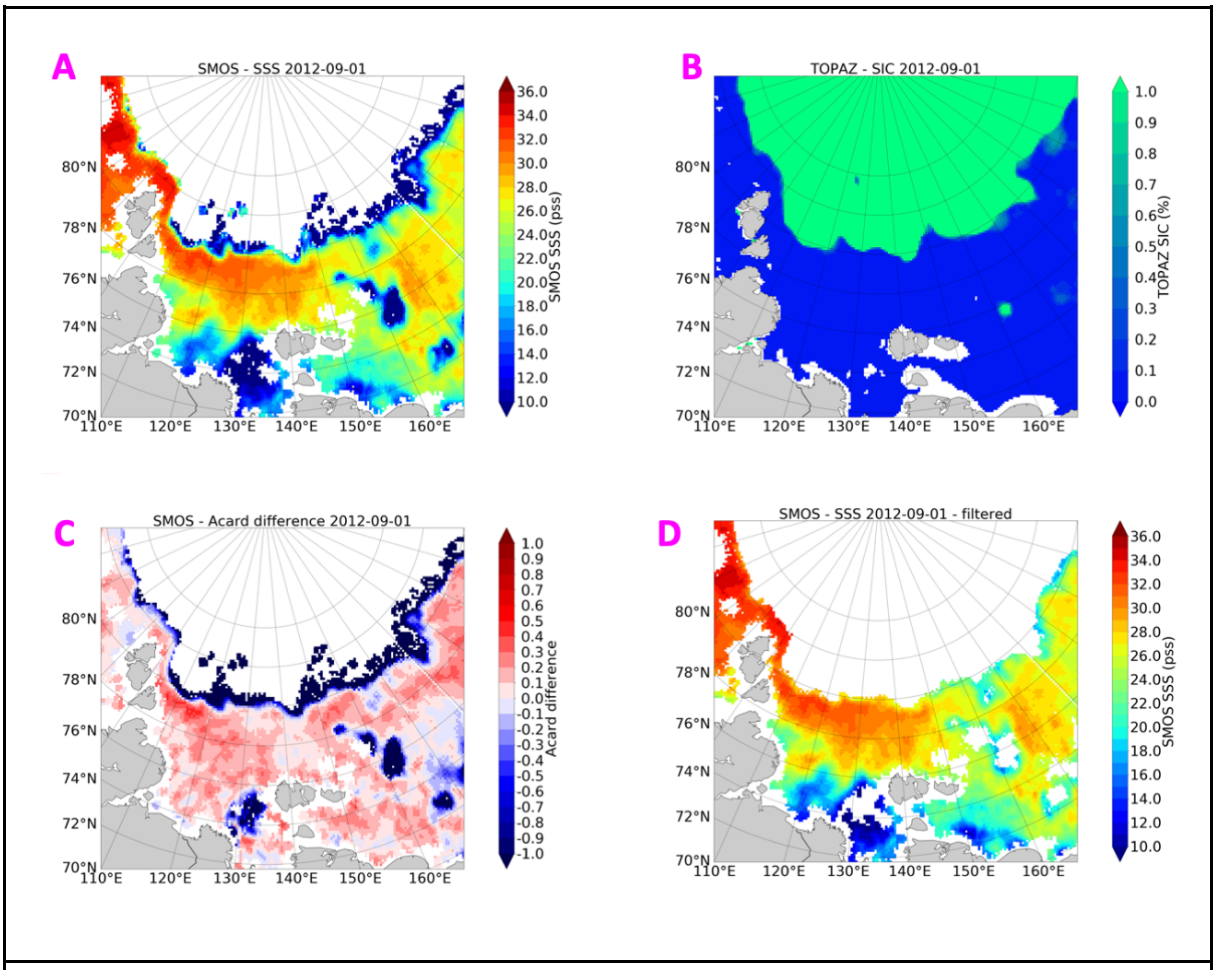

Figure 7: L3 post-processing flagging for the study case of 2012-09-01: (A) SMOS SSS pre-processed L3 estimates; (B) TOPAZ reanalysis SIC; (C) differences between $Acard_{SMOS}$ and $Acard_{KS\ (SMOS\ SSS,\ ECMWF\ SST)}$; (D) SMOS SSS estimates after filtering.

Over the whole Arctic Ocean and period investigated (Figure 8), Acard ice filtering removes all pixels with SIC larger than 2.5% and most pixels with SIC in the range of 0%-

2.5%. MoD and STDD with respect to in-situ SSS significantly decrease after filtering and do not show a dependency to TOPAZ SIC anymore suggesting that the remaining SMOS pixels are not significantly polluted by sea ice. These results demonstrate the efficiency of Acard ice filtering over using an external SIC product. Hereafter, we refer to SSS_{SMOS} as the SMOS SSS obtained after the above described processing. SSS_{SMOS} considered in the following are therefore sea ice filtered.

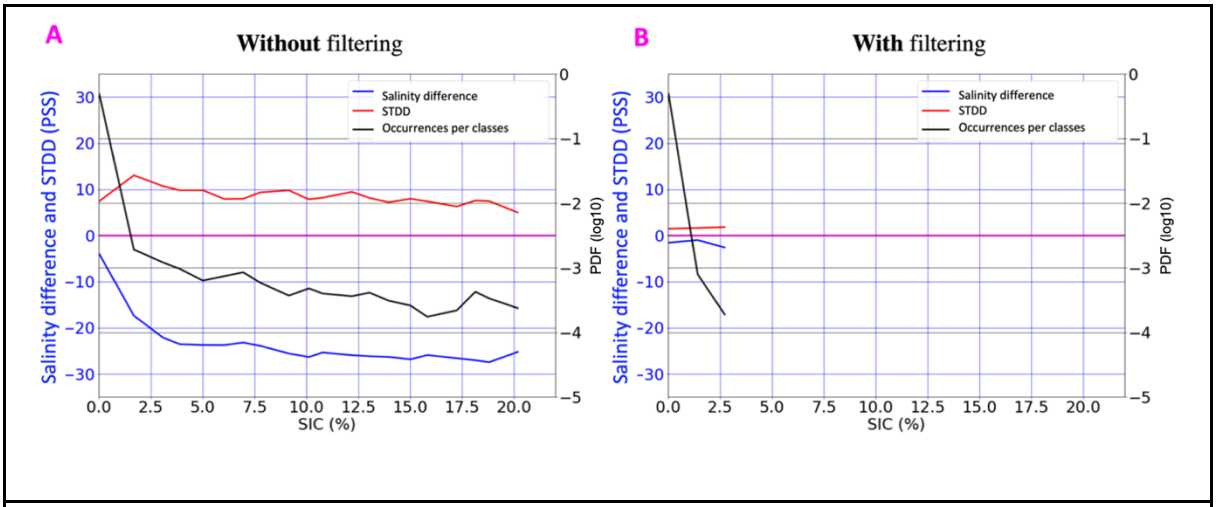

Figure 8: Mean difference and STDD between SMOS SSS and in-situ salinity and PDF of collocations per bin (bin size: 1%) of TOPAZ SIC; (A) without filtering; (B) with filtering.

5.2. Validation of the SSS product

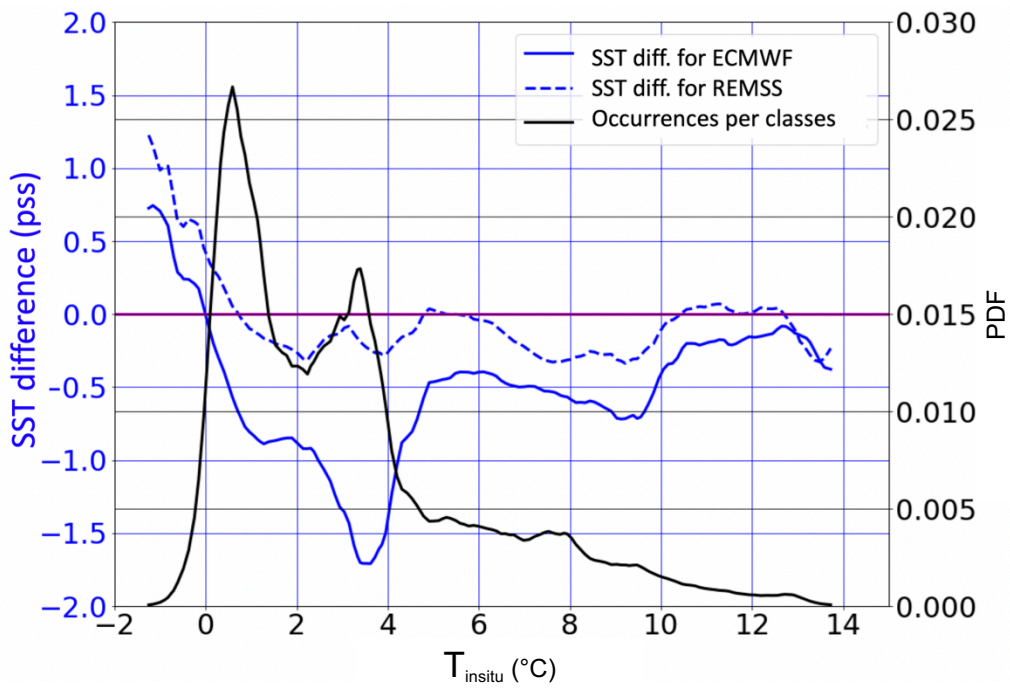

Figure 9: Difference of $SST_{ECMWF} - T_{insitu}$ (blue line) and SST_{REMSS} - T_{insitu} (blue dashed line) as a function of T_{insitu}. Distribution of T_{insitu} (black line); (bin size: 1 °C – sliding window).

The main motivation for the temperature-dependent correction is found in the distribution of SST. As shown in Figure 9, SST_{REMSS} are closer to in-situ SST than SST_{ECMWF}. Depending on the Arctic Ocean regions considered, two modes are generally present in both the distribution of SST_{REMSS} and in-situ SST (Figure 10 and 11) but the mode corresponding to higher temperatures is almost absent in the SST_{ECMWF} distribution.

In order to make a realistic comparison of the statistical distributions of SMOS and in situ SSS, in each area we add noise to S_{insitu} to mimic SMOS noise, considering a Gaussian noise being derived from the theoretical uncertainty of the collocated SMOS L3 SSS.

The positive effect of the correction is clear in Chukchi and Laptev Seas. For these two regions, SST_{ECMWF} distribution clearly underestimates the warmest SST mode (Figures 10H, I) in comparison with REMSS, or, T_{insitu}. This results into a distribution of SMOS SSS without the SST_{REMSS} correction showing an important number of underestimated SMOS SSS (Figure 10B, C). This correction results in a distribution of SMOS SSS closer to the S_{insitu} distribution

(Figures 10E, F), thus the STDD and MoD decrease and the correlation coefficient (r) increases (Table 2) for the Chukchi Sea and the Laptev Sea.

To a lower extent, the same kind of difference is observed in the Beaufort Sea (Figures 10A, D, G). In the Barents Sea, the SST_{ECMWF} distribution is closer to that of T_{insitu} and SST_{REMSS} than for the other study areas and our correction only brings a very small improvement (Figures 11A, D, G and STDD in Table 1). Finally, the Atlantic area presents a degradation of SSS after Acard difference and SST corrections (Figures 11B, E, H and STDD in Table 2). This is mainly due to the Acard correction (Appendix-E). Indeed, this correction assumes that error in the SSS estimation comes from errors in dielectric constant model and/or from erroneous prior SST. In the Atlantic area, RFI likely disturb TB such that their angular variation cannot be described with a Fresnel model, and therefore our correction is not appropriate.

Considering the whole Arctic Ocean (Figures 11C, F, I), the distribution of the corrected SMOS SSS fits better S_{insitu}. After correction, the STDD and MoD improve from 1.46 pss to 1.28 pss and from -1.54 pss to -0.27 pss, respectively; r increases from 0.92 to 0.94 (Table 2).

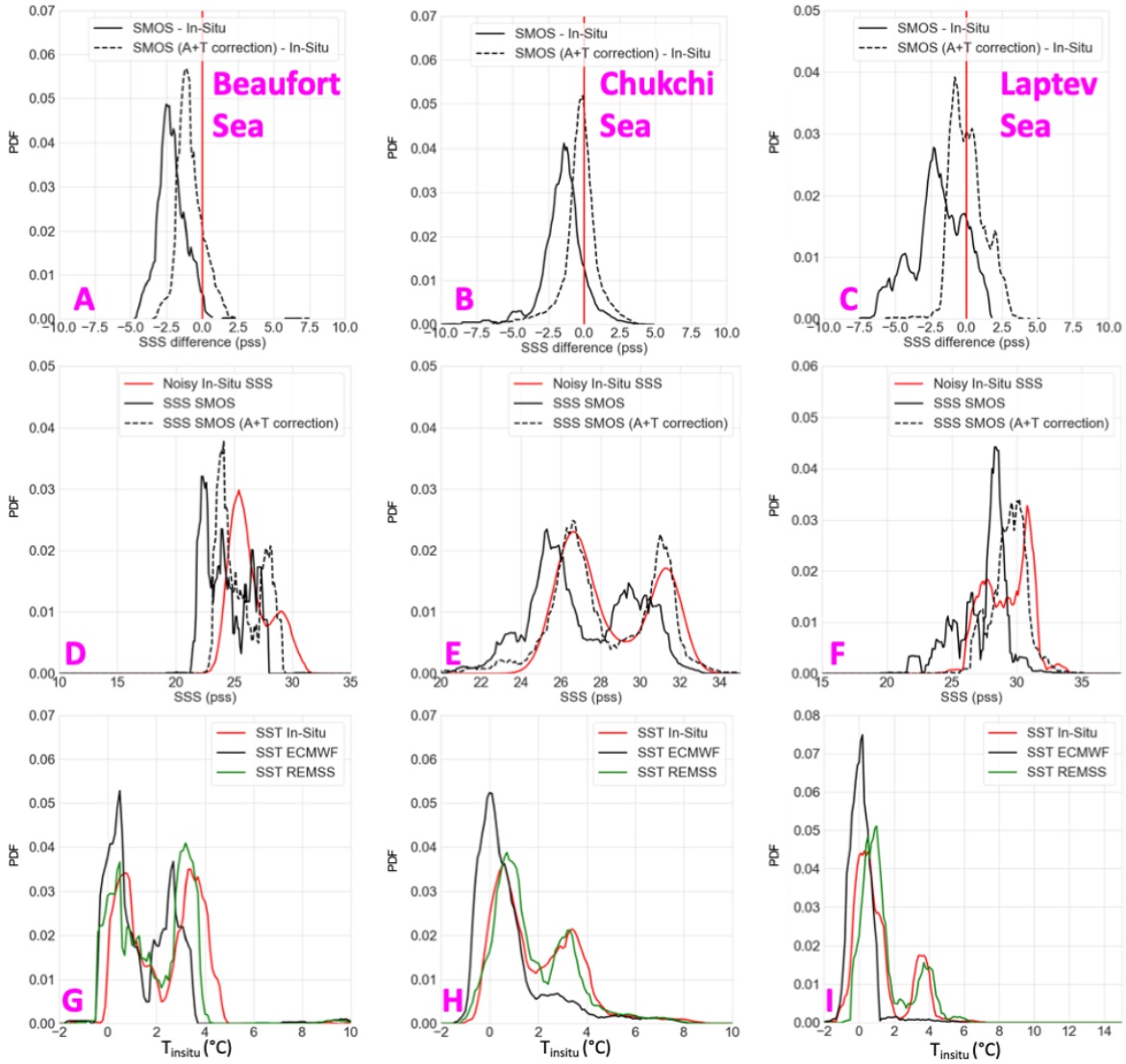

Figure 10: (A, B, C) Distribution of SMOS SSS minus S_{insitu} without correction (black line) and with correction (dashed line) for the different study areas and for the whole Arctic Ocean (1 pss SSS difference bin – sliding window); (D, E, F) distribution of SSS_{SMOS} (black line), $SSS_{SMOS\ A+T}$ (dashed line) and noisy (using SSS_{SMOS} theoretical uncertainty) S_{insitu} (red line) for the different study areas and for the whole Arctic Ocean (1 pss salinity bin – sliding window); (G, H, I) In-Situ (red), ECMWF (black) and REMSS (green) SST distributions (1 °C SST bin – sliding window). Low salinity study areas: (A, D, G): Beaufort Sea; (B, E, H): Chukchi Sea; (C, F, I) Laptev Sea.

423

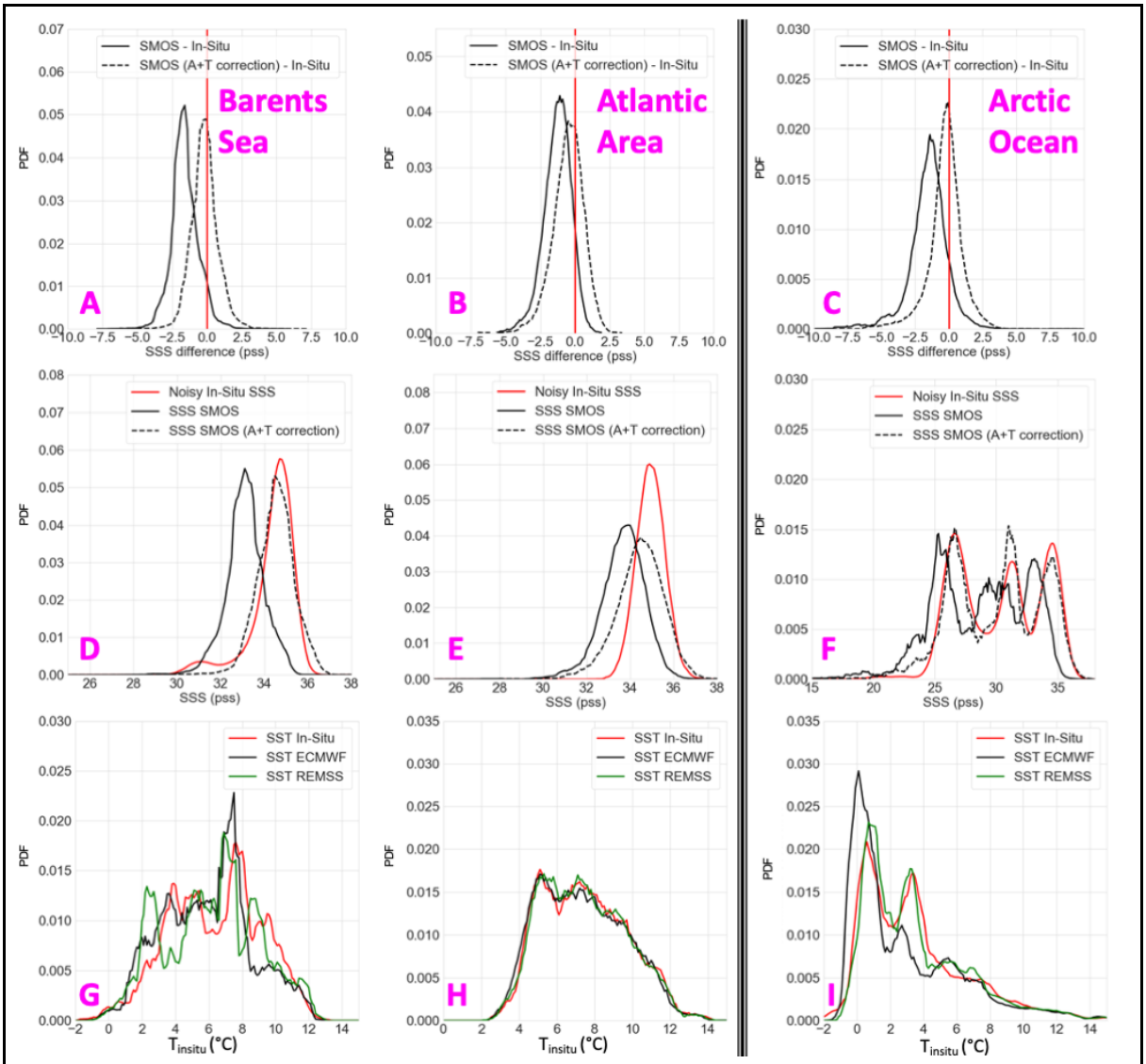

Figure 11: (A, B, C) Distribution of SMOS SSS minus S_{insitu} without correction (black line) and with correction (dashed line) for the different study areas and for the whole Arctic Ocean (1 pss SSS difference bin – sliding window); (D, E, F) distribution of SSS_{SMOS} (black line), $SSS_{SMOS\ A+T}$ (dashed line) and noisy (using SSS_{SMOS} theoretical uncertainty) S_{insitu} (1 pss salinity bin – sliding window); (G, H, I) In-Situ (red), ECMWF (black) and REMSS (green) SST distributions (1 °C SST bin – sliding window). High salinity study areas: (A, D, G) Barents Sea, (B, E, H) Atlantic Area, and (C, F, I) the whole Arctic Ocean.

Over the whole Arctic Ocean, the difference between SST_{REMSS} and T_{insitu} is less than the difference observed between SST_{ECMWF} and T_{insitu}. The difference SST_{ECMWF} - T_{insitu} exceeds -

1 °C for T_{insitu} between 3 °C and 4 °C, temperatures that are often present in the Arctic Ocean (figures 9 and 11l). In this SST range, the correction is efficient to reduce the satellite SSS differences with respect to T_{insitu}. The overestimation of SST observed with both ECMWF and REMSS products for SST lower than 0°C (Figure 9) should lead to an overestimation of SSS (Figure 12). However, an underestimation of SSS is observed for the coldest surface temperatures without any link with SST difference, likely due to some remaining very low sea ice concentration or very near surface freshening close to sea ice unidentified with in-situ measurements.

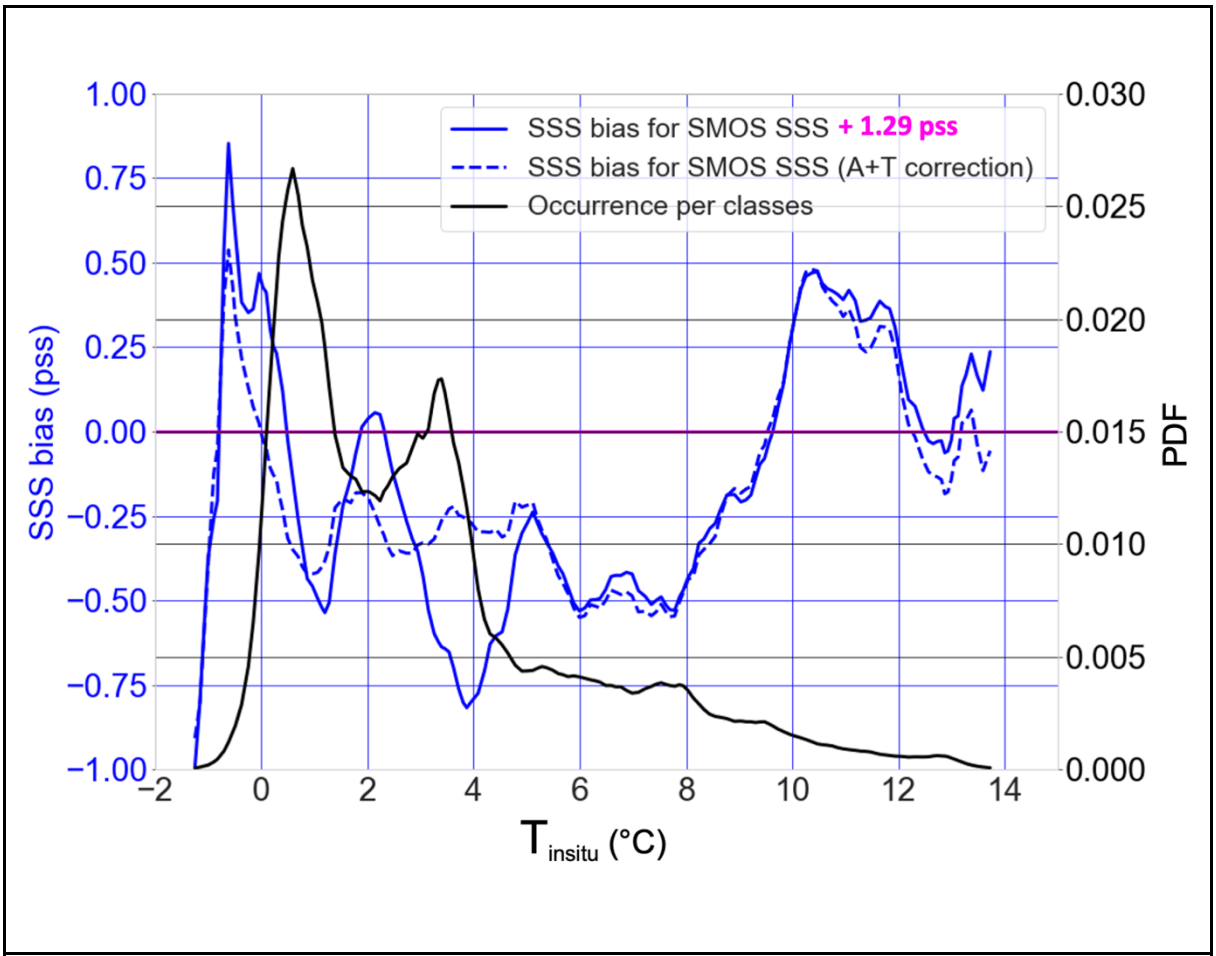

Figure 12: Averaged differences between SSS_{SMOS}+1.4pss (in order to consider the general bias) or $SSS_{SMOS\ A+T}$ and S_{insitu} and PDF of collocations per bin of in-situ SST; (bin size: 1 °C – sliding window).

435 Table 2: Comparisons between SMOS SSS, without and with correction, TOPAZ SSS and

436 S_{insitu} for the different study areas (N is the number of collocations).

Cases study	Statistic indicator	SSS_{SMOS}	$SSS_{SMOS\ A+T}$	SSS_{TOPAZ}
Beaufort Sea	MoD (pss)	-2.12	-0.83	3.67
	STDD (pss)	0.96	0.88	1.18
	r	0.86	0.88	0.86
	N	3912	3912	3912
Chukchi Sea	MoD (pss)	-1.50	-1.28	1.97
	STDD (pss)	1.47	1.23	1.78
	r	0.84	0.88	0.86
	N	90721	90721	90721
Laptev Sea	MoD (pss)	-1.97	0.11	1.51
	STDD (pss)	1.82	1.17	1.89
	r	0.53	0.75	0.04
	N	4048	4048	4048
Barents Sea	MoD (pss)	-1.59	-0.17	-0.19
	STDD (pss)	0.96	0.94	0.50
	r	-0.03	-0.04	0.19

	N	10879	10879	10879
Atlantic Area	MoD (pss)	-1.29	-0.51	0.01
	STDD (pss)	1.02	1.13	0.10
	r	0.01	-0.05	0.70
	N	2876	2876	2876
Arctic Ocean	MoD (pss)	-1.54	-0.27	1.25
	STDD (pss)	1.46	1.28	1.86
	r	0.92	0.94	0.89
	N	156986	156986	156986

6. Comparisons between SMOS SSS and TOPAZ SSS

6.1. Weekly variability

To assess the capability of the corrected SMOS SSS products to reproduce the short scale SSS variability in the Arctic relative to an ocean circulation model, we compare hereafter $SSS_{SMOS\ A+T}$ and SSS_{TOPAZ} (Table 3) to a reference salinity provided by underway TSG tracks acquired in three different seas: Greenland Sea (case study 1), Laptev Sea (case study 2) and Chukchi Sea (case study 3). For the case study in the Greenland Sea, the vessel is arriving from an area covered by sea ice. It first crosses an area of low salinity before an area with SSS ~ 35 pss. Both $SSS_{SMOS\ A+T}$ and SSS_{TOPAZ} do not reach the lower values recorded by the TSG (Figure 13A, B). Only one $SSS_{SMOS\ A+T}$ pixel reaches a value lower than 26 pss, but an effect of ice may not be excluded even if the SIC from TOPAZ indicates no ice. $SSS_{SMOS\ A+T}$ exhibits better STDD and MoD than SSS_{TOPAZ} with respect to the TSG. For the study case in the Laptev Sea

(Figure 13C and 13D), $SSS_{SMOS\ A+T}$ show a positive bias (larger than SSS_{TOPAZ}) for higher SSS values recorded by the TSG contrary to SSS_{TOPAZ} which fits well with these salinities. However, the large freshening (more than 10 pss) observed by the vessel crossing the Lena river plume is very well represented by $SSS_{SMOS\ A+T}$ contrary to SSS_{TOPAZ}, which misses the location of the river plume and its intensity. Nevertheless, $SSS_{SMOS\ A+T}$ demonstrates in this case a higher STDD than SSS_{TOPAZ}. In the Chukchi Sea (Figure 13E and 13F), the underway TSG presents a large variability also observed by $SSS_{SMOS\ A+T}$ but with some bias. This variability is not recorded by SSS_{TOPAZ}. The STDD and bias with respect in situ data, are lower with $SSS_{SMOS\ A+T}$ than with SSS_{TOPAZ} by ~ 0.2 and 0.3, respectively.

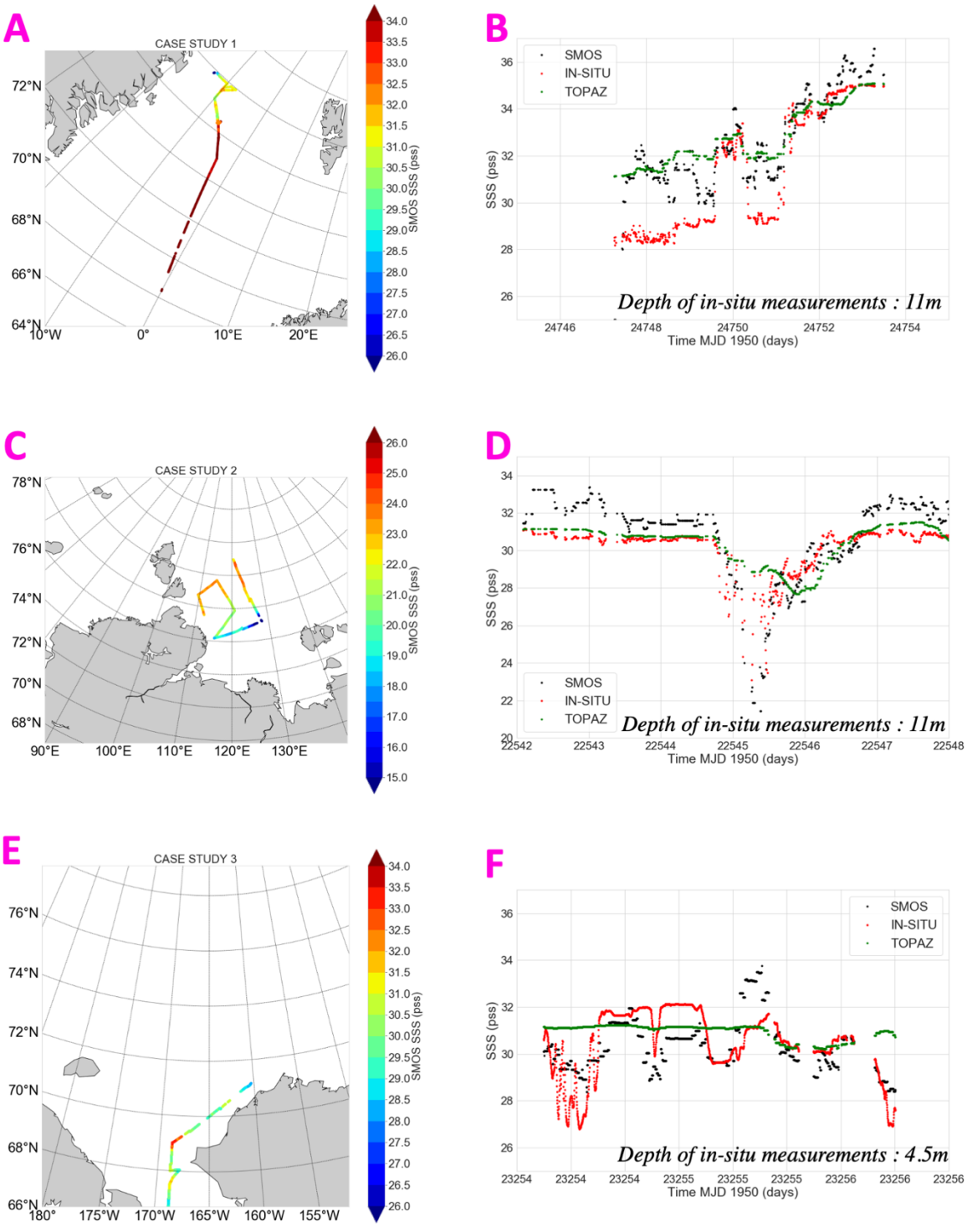

Figure 13: (A, C, E) SMOS SSS measurements collocated with underway TSG measurements; (B, D, F) Time series of SMOS SSS (black) and TOPAZ SSS (green)

collocated with underway TSG salinity measurements (red). Case studies in the Greenland Sea (A, D, G), in the Laptev Sea (B, E, H) and Chukchi Sea (C, F, I).

459

460 Table 3: MoD, STDD and r between $SSS_{SMOS\ A+T}$ or TOPAZ SSS and in-situ measurements
461 for the underway TSG case studies.

Cases study	Statistic indicator	$SSS_{SMOS\ A+T}$	SSS_{TOPAZ}
Case study 1	MoD (pss)	1.25	1.41
	STDD (pss)	1.27	1.43
	r	0.88	0.96
Case study 2	MoD (pss)	0.59	0.25
	STDD (pss)	1.37	0.98
	r	0.84	0.69
Case study 3	MoD (pss)	-0.15	0.51
	STDD (pss)	1.24	1.43
	r	0.56	0.12

462 In Figure 14, $SSS_{SMOS\ A+T}$ and SSS_{TOPAZ} distributions are compared with S_{insitu}
463 distributions over the whole Arctic Ocean. The distribution of $SSS_{SMOS\ A+T}$ compares very well
464 with the distribution of S_{insitu} (Figure 14A). One mode of the S_{insitu} distribution (lower SSS) is
465 totally absent in the SSS_{TOPAZ} distribution. STDD (Table 2) is 1.28 pss for $SSS_{SMOS\ A+T}$ and
466 1.86 pss for SSS_{TOPAZ}. r reaches 0.94 with $SSS_{SMOS\ A+T}$ while it is 0.89 with SSS_{TOPAZ}. The

distribution of errors for $SSS_{SMOS\ A+T}$ presents only one mode contrary to SSS_{TOPAZ} that present two modes due to the absence of the lower SSS (Figure 14B).

The scatterplot of $SSS_{SMOS\ A+T}$ versus S_{insitu} further indicates an overall agreement between SSS estimates from space and in-situ measurements. In addition, the SMOS SSS uncertainty estimated in the L3 product (see section 2.1.2) seems to be a good indicator of the quality of the considered $SSS_{SMOS\ A+T}$ estimate.

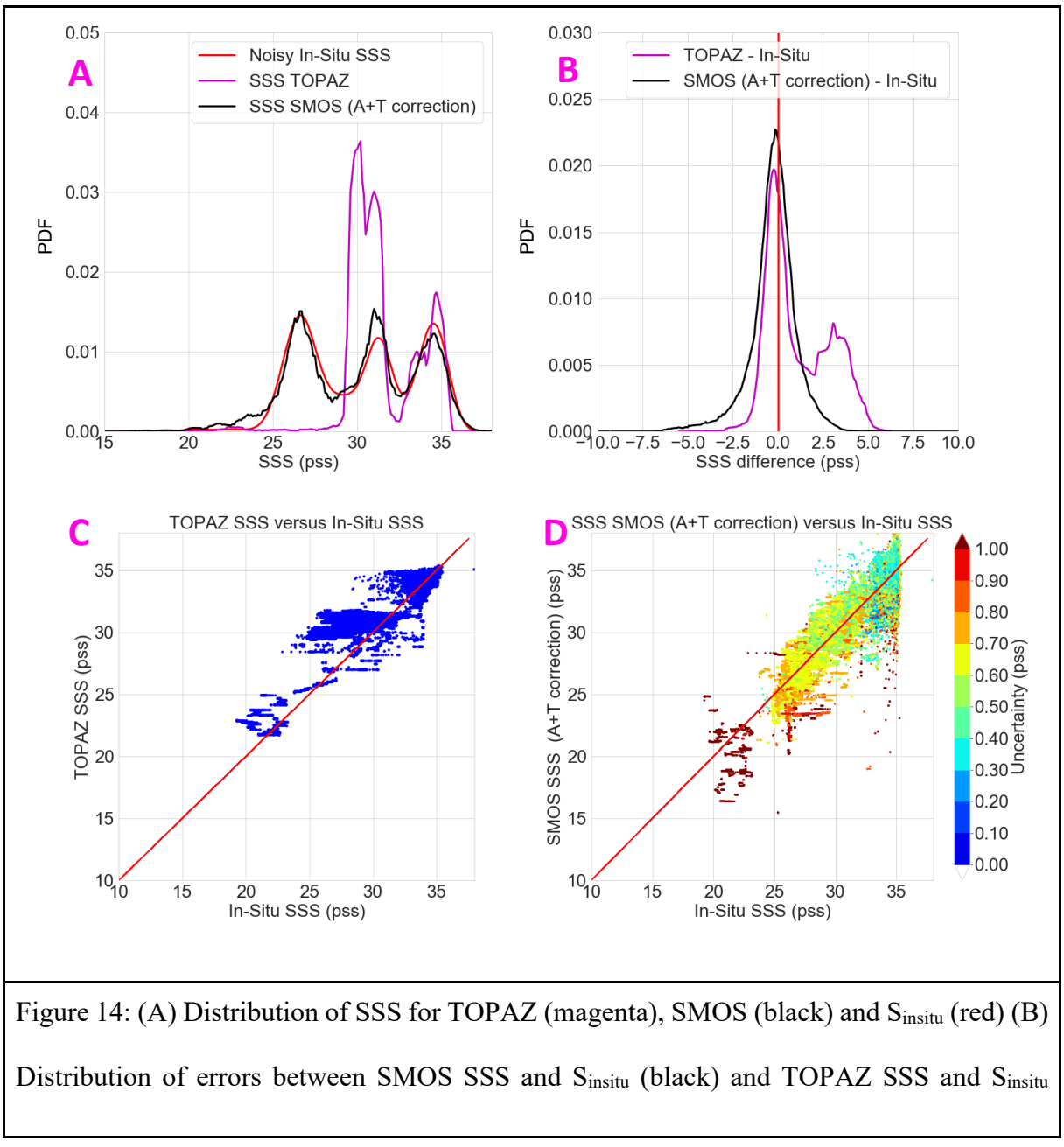

Figure 14: (A) Distribution of SSS for TOPAZ (magenta), SMOS (black) and S_{insitu} (red) (B) Distribution of errors between SMOS SSS and S_{insitu} (black) and TOPAZ SSS and S_{insitu}

(magenta) (C) Scatterplot of TOPAZ SSS versus S_{insitu}; (D) Scatterplot of SMOS SSS versus S_{insitu} with SMOS theoretical uncertainty coded in color.

473

474 6.2. Interannual variability

475 We then compare the $SSS_{SMOS\ A+T}$ interannual variability to SSS_{TOPAZ} interannual
476 variability. For each year between 2011 to 2017 we average SSS between August and October
477 in order to consider the season with the lowest sea ice coverage in the Arctic Ocean. The average
478 is weighted by the uncertainty value of each L3 SSS estimate. Figure 15 is a comparison for the
479 2012, 2013 and 2014 years and Figure 16 is a comparison for the 2015, 2016 and 2017 years.
480 Contrary to TOPAZ that provides an SSS value for each pixel of the Arctic Ocean, SSS_{SMOS}
481 $_{A+T}$ coverage depends on the sea ice extent. For the comparison we take into account SSS_{TOPAZ}
482 only when a $SSS_{SMOS\ A+T}$ value exists.

483 A good overall consistency in the Arctic Ocean is observed between $SSS_{SMOS\ A+T}$ and
484 SSS_{TOPAZ} interannual variations. However, $SSS_{SMOS\ A+T}$ exhibits a higher interannual and
485 spatial variability than SSS_{TOPAZ}. Furthermore, some areas behave differently with $SSS_{SMOS\ A+T}$
486 in comparison with SSS_{TOPAZ}. For the whole period and as observed previously regarding S_{insitu}
487 (Table 2), the freshening of the Beaufort gyre is strongly underestimated with SSS_{TOPAZ}
488 compared to $SSS_{SMOS\ A+T}$. The variability and spatial extent of Arctic Ocean river plumes also
489 differ strongly between SSS_{TOPAZ} and $SSS_{SMOS\ A+T}$. In the Kara Sea, the locations and strength
490 of the Ob and the Yenissei river plumes are highly variable from one year to the other
491 (freshening minimum in 2012 and 2016, maximum in 2015). This variability is captured by
492 SSS_{TOPAZ} and $SSS_{SMOS\ A+T}$, but with larger amplitudes in $SSS_{SMOS\ A+T}$, in particular in 2015.
493 River plume propagation to the north or/and to the east in the East-Siberian Sea are not captured
494 in the same way by SSS_{TOPAZ} and $SSS_{SMOS\ A+T}$. For example, in 2015, the strong northward
495 advection of Lena river plume shown by $SSS_{SMOS\ A+T}$ is not observed with SSS_{TOPAZ}. Similar

observations are made in the Bering strait with the entry of Pacific water or low SSS water in the Greenland Sea and in the Baffin Bay.

Contrary to SSS_{TOPAZ}, freshening patterns are observed at the northern boundary of the field covered by $SSS_{SMOS\ A+T}$ (limitation due to the presence of permanent ice). The cause of this freshening is not totally explained and may come from a real freshening due to ice melting or an imprint of sea ice due to an imperfect filtering of sea ice.

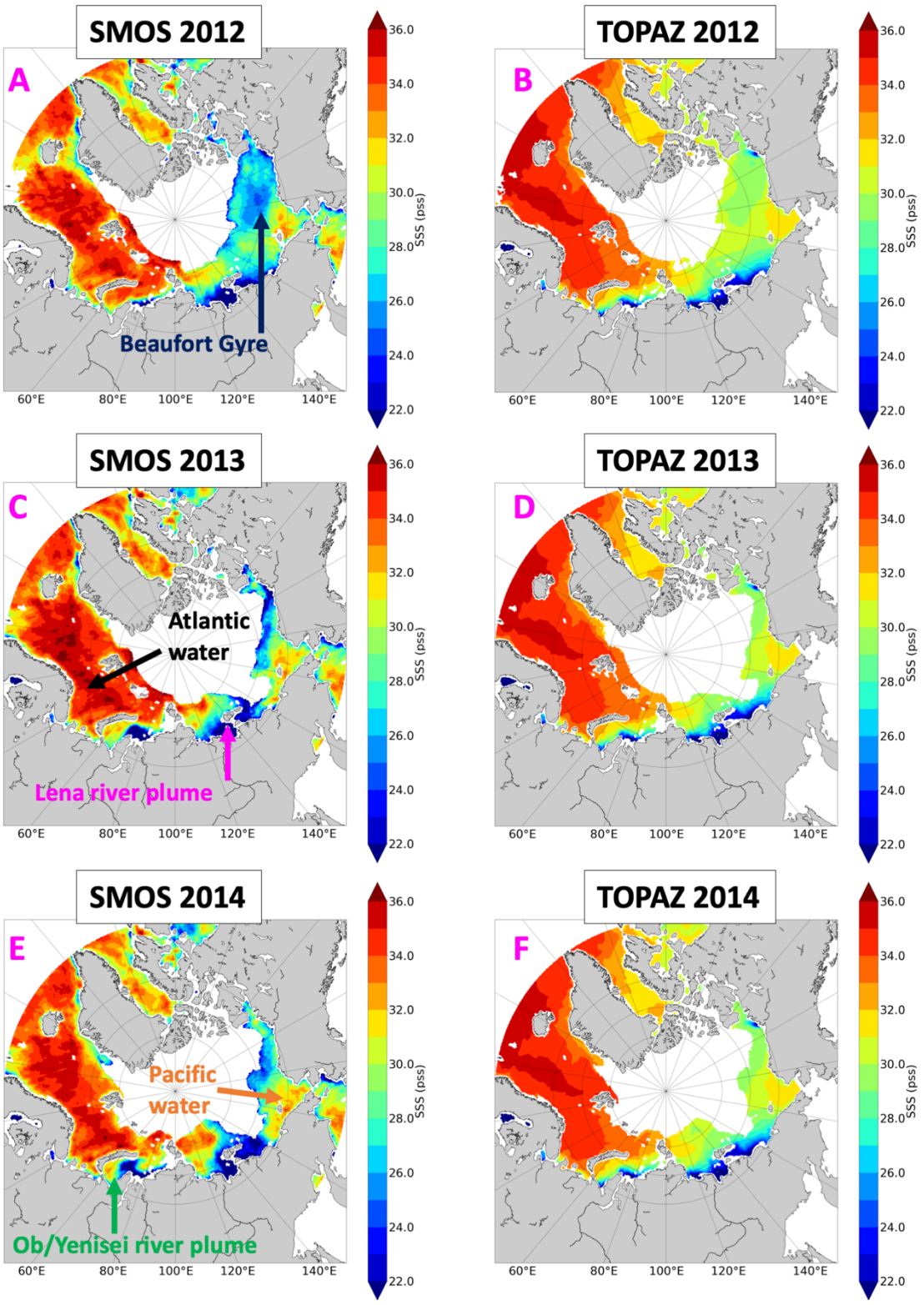

Figure 15: SSS average for the period from August to October for year 2012, 2013 and 2014; (left column) $SSS_{SMOS\ A+T}$; (right column) SSS_{TOPAZ}.

502

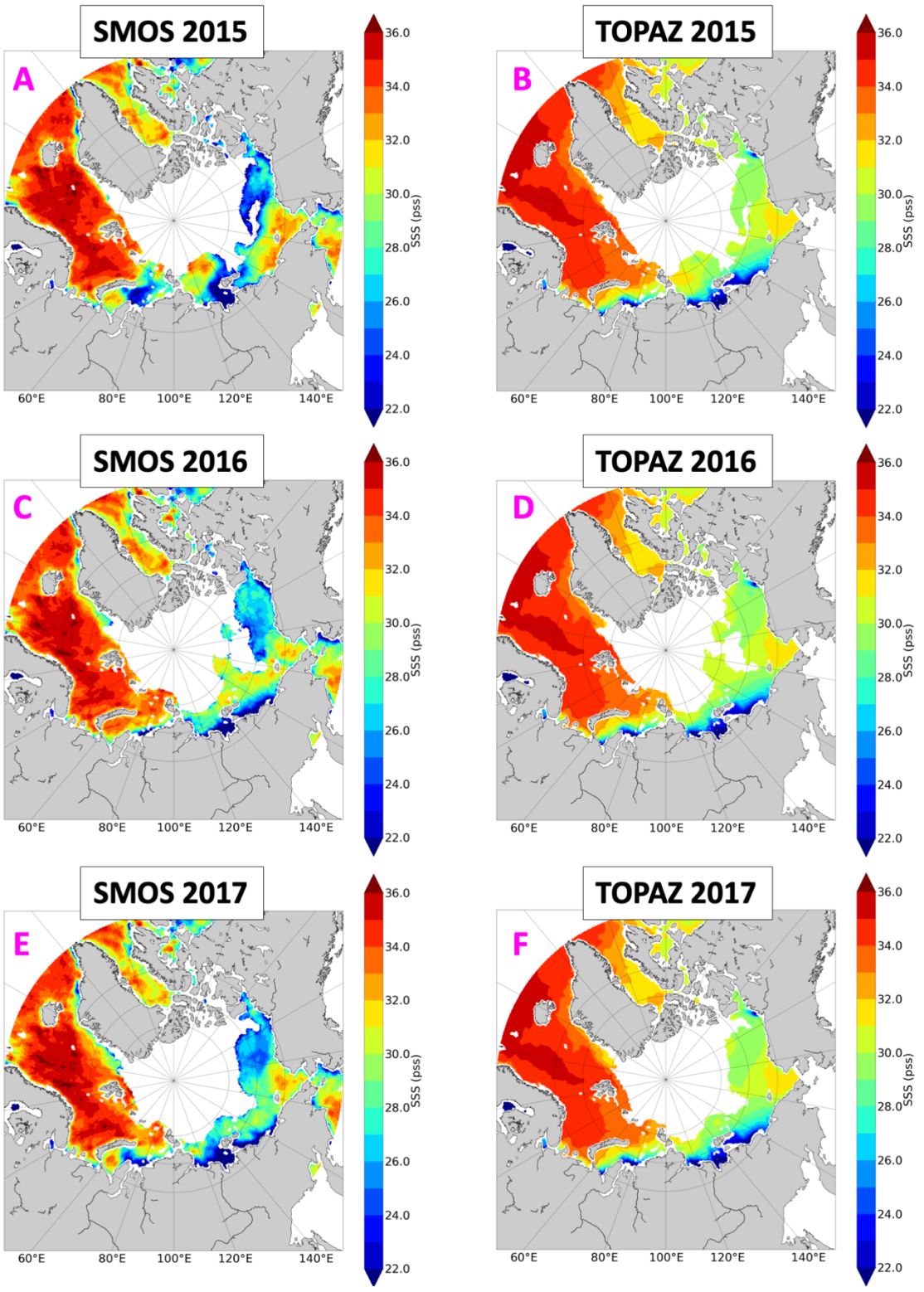

Figure 16: SSS average from August to October for year 2015, 2016 and 2017; (left column) $SSS_{SMOS\ A+T}$; (right column) SSS_{TOPAZ}.

7. Conclusion and discussion

We present a methodology that significantly improves SSS estimates in the Arctic Ocean. It is applied to SMOS L3 SSS derived from ESA level 2 operational processing (L2 OS v662).

In a first step, the difference between a pseudo dielectric constant, Acard, retrieved from SMOS measurements and a theoretical Acard estimated with KS model is used to efficiently filter out biased SSS in pixels partially covered by sea ice.

A global correction (1.29 pss) over the whole Arctic Ocean is applied, to take into account the uncertainty associated with the absolute calibration of the measurements.

The Acard difference is then used as a metric of the biases in the KS model for the dielectric constant of sea water. An additional SST correction derived using an external SST satellite product, SST_{REMSS}, is performed. The latter is motivated by observed difference of statistical distribution between SST_{ECMWF} (which is used in the retrieval of SSS) and T_{insitu}. The correction strongly improves the SMOS SSS estimate. This relies on the importance of correcting prior SST in cold regions where the sensitivity of TB to SSS is low. The effect of the SST correction is particularly noticeable in the Arctic Seas where river inflows generate strong SST gradients associated with strong SSS gradients: after this SST correction the SSS variability becomes much closer to the observations (Figure 14a).

Our correction makes use of SST_{REMSS} obtained by merging microwave and IR SST. The use of the REMSS "microwave only" OI SST gives very close statistical results (Appendix-F). Nevertheless, statistics obtained with SST_{REMSS} "microwave only" are slightly better for two reasons: 1/ the sea ice filtering of SST_{REMSS} "microwave only" is more stringent than the one of SST_{REMSS} and, in some cases, than the one based on SMOS Acard; 2/ SST_{REMSS} "microwave only" are not provided too close from the coast where SSS uncertainty is higher.

Our correction does not reveal the complexity of biases resulting from land/sea contrast, but land/sea bias correction in the Arctic Ocean is a challenging issue that needs to be investigated in further studies. It is likely one of the reasons why SSS calibration needs to be adjusted. Another limitation of the correction methodology is that we only consider issues with SST and dielectric constant model : surface roughness effects linked to e.g. wind in limited fetch areas or to surfactants could also play a role, but these effects were out of the scope of our study.

The quality of our new product is assessed by comparison with various in-situ measurements (Argo, Underway TSG and CTD casts) and with an ocean model outputs (TOPAZ). In-situ measurements cover a large range of SSS. The in-situ salinity measurement depth (between 1 m and 10 m) is shown to have a strong impact on the difference between SSS_{SMOS} and S_{insitu}, especially in low SSS areas (e.g., rivers plumes) that are often very stratified in salinity close to the surface. Hence only S_{insitu} between 1m and 5m depth are retained for the validation.

The corrected SSS better performs than TOPAZ reanalysis, essentially in areas of large temporal and spatial variability. Over the whole Arctic Ocean, STDD between weekly corrected SMOS SSS and S_{insitu} is of 1.28 pss, while STDD between TOPAZ SSS and S_{insitu} is of 1.86 pss. The statistics of the comparisons with S_{insitu} in the various regions (the Beaufort, Chukchi, Laptev and Barents Seas, and an Atlantic Area) are more stable from one study area to another with corrected SMOS SSS than with TOPAZ SSS. SMOS STDD vary between 0.94 pss and 1.23 pss, while TOPAZ STDD vary between 0.50 pss and 1.89 pss. The mean differences obtained with SMOS SSS vary between -1.28 pss and 0.11 pss while the ones obtained with TOPAZ SSS vary between -0.19 pss and 3.67 pss. SMOS SSS captures high variability in fresh Arctic Seas with a favorable signal to noise ratio as shown by high correlation levels on the

551 order of 0.8 between SMOS SSS and in-situ S_{insitu}. It is not the case in less variable salty Arctic
552 Seas (Table 2).

553 While collocations with in-situ measurements, in particular underway TSG from research
554 vessel, demonstrates SMOS ability to capture SSS (temporal and spatial) variability at short
555 scale, SMOS SSS seasonal averages bring a new perspective on the SSS variability in the Arctic
556 Ocean. Compared with the TOPAZ reanalysis, it shows a larger variability in river plumes and
557 differences of pattern, e.g. in the Beaufort gyre (Figure 15 and 16). These observations suggest
558 complementarity between SMOS SSS and TOPAZ reanalysis products. This was already
559 demonstrated by Xie et al (2019) for Arctic SSS produced at the Barcelona Expert center, but
560 this is even more evident with this new product in very variable Arctic Seas (Appendix-H,
561 Laptev Sea and Beaufort Sea).

562 The presented SSS product demonstrates valuable performances compared to other SSS
563 products in Arctic Ocean (Appendix-H). It provides avenues for improvement in the ESA L2
564 OS processor concerning the detection of sea ice, the correction of dielectric constant and SST
565 related flaws. Moreover, additional work is needed in areas with lower SSS variability and RFI
566 contamination as in the North Atlantic. In addition to the methods presented in this study, a
567 correction for the land/sea contamination and the latitudinal biases as presented by Boutin et al
568 (2018) or/and an optimal interpolation using complementarity between SMOS SSS and in-situ
569 measurements could further improve SSS derived from SMOS mission in the Arctic Ocean.

570 This study highlights the importance of sea ice filtering. In that respect, increasing the
571 spatial resolution of L-band interferometric radiometer measurements to 10 km, as proposed by
572 the SMOS-HR project (Rodríguez-Fernández et al., 2019), would greatly help to better filter
573 the ocean areas partially covered by sea ice and would allow to get closer to the ice edge and to
574 land.

This study highlights the importance of using an SST prior consistent with L-Band radiometric measurement for SSS retrieval in the Arctic Ocean. Ideally, the prior SST should be measured at the same spatial resolution and at the same time as the L-band measurement. One of the major CIMR (Copernicus Image Microwave Radiometer, Kilic et al., 2018) mission goal over the ocean is to provide simultaneous SSS and SST measurements but at different spatial resolution (SSS from the L-Band TB at ~60 km resolution and SST from the C/X-band channels at ~15 km). Joined and simultaneous SSS/SST estimates at the same resolution than the L-Band channel, i.e., 36x60 km^2 will therefore be available from this sensor but at a rather low spatial resolution for the estimate of the SSS field. Complementarily, SMOS-HR interferometric mission goal is to provide L-Band TB and therefore SSS at a spatial resolution (~10 km) close to CIMR SST resolution but it won't include an independent SST sensor. Hence combining measurements from both missions would very likely improve SSS fields estimates in the Arctic Ocean.

This study is limited to the analysis of SSS provided by the SMOS satellite mission in the Arctic Ocean. Nevertheless, during the period considered in this study, two other satellite missions, SMAP and Aquarius, have monitored SSS over the global ocean. The CCI+SSS project run as a part of ESA Climate Change Initiative aims at generating improved and consistent multi-satellites SSS fields and should bring a decisive improvement to the level 4 SSS maps, especially in the Arctic Ocean due to the short revisit time allowed by the orbit configuration of these satellites. The avenue for SMOS processing improvement that we propose should also benefit to the CCI+SSS products that incorporate SMOS measurements.

Acknowledgments

AS is supported by a SU Ph. D. grant. This work was supported by CNES-TOSCA 'SMOS-Ocean', CNES Centre Aval de Traitement des Données SMOS (CATDS) and ESA 'Expert

Support Laboratory for level 2 Ocean Salinity' projects. AT acknowledges financial support from the Ministry of Science and Higher Education of the Russian Federation, project RFMEFI61617X0076.

References

Björk, G. 2017. CTD data from the SWERUS-C3 expedition 2014 in the Arctic Ocean. PANGAEA, https://doi.org/10.1594/PANGAEA.884144.

Brucker, L., Dinnat, E. P., and Koenig, L. S. 2014. Weekly gridded Aquarius L-band radiometer/scatterometer observations and salinity retrievals over the polar regions, Part 2: Initial product analysis, The Cryosphere, 8, 3, 915—930, https://www.the-cryosphere.net/8/915/2014/, doi:10.5194/tc-8-915-2014.

Boutin, J., Chao, Y., Asher, W.E., Delcroix, T., Drucker, R., Drushka, K., Kolodziejczyk, N., Lee, T., Reul, N., Reverdin, G., Schanze, J., Soloviev, A., Yu, L., Anderson, J., Brucker, L., Dinnat, E., Santos-Garcia, A., Jones, W.L., Maes, C., Meissner, T., Tang, W., Vinogradova, N., Ward, B. 2016. Satellite and In Situ Salinity: Understanding Near-Surface Stratification and Subfootprint Variability. Bull. Amer. Meteor. Soc., 97, 1391–1407, https://doi.org/10.1175/BAMS-D-15-00032.1

Boutin, J., Vergely, J. L., Marchand, S., D'Amico, F., Hasson, A., Kolodziejczyk, N., Reul, N., Reverdin, G., and Vialard, J. 2018. New SMOS Sea Surface Salinity with reduced systematic errors and improved variability, Remote Sens. Environ., 214, 115–134, https://doi.org/10.1016/j.rse.2018.05.022.

Carmack, E. C., The alpha/beta ocean distinction: A perspective on freshwater fluxes, convection, nutrients and productivity in high-latitude seas, Deep Sea Research Part II: Topical Studies in Oceanography, Volume 54, Issues 23–26, 2007, Pages 2578-2598, ISSN 0967-0645, https://doi.org/10.1016/j.dsr2.2007.08.018.

625 Carmack, E. C., et al. 2016. Freshwater and its role in the Arctic Marine System : Sources,
626 disposition, storage, export, and physical and biogeochemical consequences in the Arctic and
627 global oceans, J. Geophys. Res. Biogeosci., 121, 675–717, doi:10.1002/2015JG003140.
628 Chassignet, E.P., Hurlburt, H.E., Metzger, E.J., Smedstad, O.M., Cummings, J.A., Halliwell,
629 G.R., Bleck, R., Baraille, R., Wallcraft, A.J., Lozano, C., Tolman,H.L., Srinivasan, A., Hankin,
630 S., Cornillon, P., Weisberg, R., Barth, A., He, R., Werner, F., Wilkin, J. 2009. US GODAE:
631 Global ocean prediction with the HYbrid Coordinate Ocean Model (HYCOM). Oceanography
632 22(2):64–75, doi:10.5670/oceanog.2009.39.
633 Dinnat, E. P., Le Vine, D. M., Boutin, J., Meissner, T., Lagerloef, G. 2019. Remote Sensing,
634 2072-4292, 11, 7, 750, Remote Sensing of Sea Surface Salinity: Comparison of Satellite and In
635 Situ Observations and Impact of Retrieval Parameters, doi:10.3390/rs11070750,
636 https://www.mdpi.com/2072-4292/11/7/750.
637 Donlon, C.J., Martin, M., Stark, J., Roberts-Jones, J., Fiedler, E., Wimmer, W. 2012. The
638 operational sea surface temperature and sea ice analysis (OSTIA) system. RemoteSens.
639 Environ. 116, 140–158.https://doi.org/10.1016/j.rse.2010.10.017.
640 ECMWF. 2016. IFS Documentation CY41R2. Part II : Data Assimilation. IFS Documentation.
641 ECMWF.
642 Font, J., Camps, A., Borges, A., Martin-Neira, M., Boutin, J., Reul, N.,Kerr, Y. H., Hahne, A.,
643 Mecklenburg, S. 2010. SMOS: The Challenging Sea Surface Salinity Measurement From
644 Space, Proceedings of the IEEE, 98(5), 649-665, doi:10.1109/jproc.2009.2033096.
645 Haine, T. W., Curry, B., Gerdes, R., Hansen, E., Karcher, M., Lee, C., Rudels, B. , Spreen, G. ,
646 de Steur, L. , Stewart, K. D. and Woodgate, R. 2015. Arctic freshwater export: Status,
647 mechanisms, and prospects, Global and Planetary Change, 125, pp. 13-35. doi:
648 10.1016/j.gloplacha.2014.11.013.

649 Høyer J.L., Karagali, I., Dybkjær, G., Tonboe, R., Multi sensor validation and error
650 characteristics of Arctic satellite sea surface temperature observations, Remote Sensing of
651 Environment, Volume 121, 2012, Pages 335-346, ISSN 0034-4257,
652 https://doi.org/10.1016/j.rse.2012.01.013.
653 IPCC, 2018: Summary for Policymakers. In: Global warming of 1.5°C. An IPCC Special
654 Report on the impacts of global warming of 1.5°C above pre-industrial levels and related global
655 greenhouse gas emission pathways, in the context of strengthening the global response to the
656 threat of climate change, sustainable development, and efforts to eradicate poverty [V. Masson-
657 Delmotte, P. Zhai, H. O. Pörtner, D. Roberts, J. Skea, P. R. Shukla, A. Pirani, W. Moufouma-
658 Okia, C. Péan, R. Pidcock, S. Connors, J. B. R. Matthews, Y. Chen, X. Zhou, M. I. Gomis, E.
659 Lonnoy, T. Maycock, M. Tignor, T. Waterfield (eds.)]. World Meteorological Organization,
660 Geneva, Switzerland, 32 pp.
661 Ivanov V et al. 2013. NABOS 2013 Arctic Expedition aboard RV "Akademik Fedorov",
662 https://nabos.iarc.uaf.edu/NABOS2/data/registered/2013/metadata/brief_report_2013-
663 engl.pdf.
664 JAMSTEC (2013) MIRAI MR12-E03 Cruise Data. JAMSTEC. doi:10.17596/0001847
665 (accessed 2019-07-16).
666 JAMSTEC (2013) MIRAI MR13-06 Leg1 Cruise Data. JAMSTEC. doi:10.17596/0001856
667 (accessed 2019-07-16).
668 JAMSTEC (2015) MIRAI MR14-05 Cruise Data. JAMSTEC. doi:10.17596/0001861
669 (accessed 2019-07-16).
670 Kerr, Y. H., et al. 2010. The SMOS Mission : New Tool for Monitoring Key Elements of the
671 Global Water Cycle, Proceedings of the IEEE, 98(5), 666-687.
672 Kilic, L., Prigent, C., Aires, F., Boutin, J., Heygster, G., Tonboe, R. T. et al. 2018. Expected
673 performances of the Copernicus Imaging Microwave Radiometer (CIMR) for an all-weather

674 and high spatial resolution estimation of ocean and sea ice parameters. Journal of Geophysical
675 Research: Oceans, 123, 7564– 7580. https://doi.org/10.1029/2018JC014408
676 Klein, L.A. and Swift, C.T. 1977. An Improved Model for the Dielectric Constant of Sea Water
677 at Microwave Frequencies. IEEE Journal of Oceanic Engineering, 2, 104-
678 111. http://dx.doi.org/10.1109/JOE.1977.1145319.
679 Köhler, J., Sena Martins, M., Serra, N., Stammer, D. 2015. Quality assessment of spaceborne
680 sea surface salinity observations over the northern North Atlantic, J. Geophys. Res. Oceans,
681 120, 94–112, doi:10.1002/ 2014JC010067.
682 Lagerloef, G., et al. 2008) The Aquarius/SAC-D mission: Designed to meet the salinity remote
683 sensing challenge Oceanography, 21(1), 68–81. Lind, S., Ingvaldsen, R. B., Furevik, T., 2018.
684 Arctic warming hotspot in the northern Barents Sea linked to declining sea-ice import. Nature
685 Climate Change. https://doi.org/10.1038/s41558-018-0205-y.
686 Makhotin, M., Ivanov, V. 2018. Physical oceanography measured with CTD/Watersampler-
687 system during PU2012 to the Barents Sea in
688 2012. PANGAEA, https://doi.org/10.1594/PANGAEA.895269.
689 Makhotin, M., Ivanov, V. 2018. Physical oceanography measured with CTD/Watersampler-
690 system during PU2013 to the Barents Sea in
691 2013. PANGAEA, https://doi.org/10.1594/PANGAEA.895270.
692 Makhotin, M., Ivanov, V. 2018. Physical oceanography measured with CTD/Watersampler-
693 system during PU2014 to the Barents Sea in
694 2014. PANGAEA, https://doi.org/10.1594/PANGAEA.895271.
695 Marquardt, D. W., "An algorithm for least-squares estimation of non-linear parameters," J. Soc.
696 Ind. Appl. Math, vol. 11, pp. 431-441, 1963.
697 Matsuoka, A., Babin, M., Devred E. C. 2016. A new algorithm for discriminating water sources
698 from space: A case study for the southern Beaufort Sea using MODIS ocean color and SMOS

699 salinity data, Remote Sensing of Environment, Volume 184, Pages 124-138, ISSN 0034-4257,
700 https://doi.org/10.1016/j.rse.2016.05.006.
701 Meissner, T., Wentz, F. J., Scott, J., Vazquez-Cuervo, J. 2016. Sensitivity of Ocean Surface
702 Salinity Measurements From Spaceborne L-Band Radiometers to Ancillary Sea Surface
703 Temperature, in *IEEE Transactions on Geoscience and Remote Sensing*, vol. 54, no. 12, pp.
704 7105-7111, doi: 10.1109/TGRS.2016.2596100.
705 Olmedo, E., Gabarró, C., González-Gambau, V., Martínez, J., Ballabrera-Poy, J., Turiel, A.,
706 Portabella, M., Fournier, S., and Lee, T.2018. Seven Years of SMOS Sea Surface Salinity at
707 High Latitudes: Variability in Arctic and Sub-Arctic Regions, Remote Sens., 10, 1772,
708 https://doi.org/10.3390/rs10111772.
709 Peralta-Ferriz, C., Woodgate, R. A. 2015. Seasonal and interannual variability of pan-Arctic
710 surface mixed layer properties from 1979 to 2012 from hydrographic data, and the dominance
711 of stratification for multiyear mixed layer depth shoaling, Progress in Oceanography, Volume
712 134, Pages 19-53, ISSN 0079-6611, https://doi.org/10.1016/j.pocean.2014.12.005.
713 Piepmeier J. R. et al. 2017. SMAP L-Band Microwave Radiometer : Instrument Design and
714 First Year on Orbit," in IEEE Transactions on Geoscience and Remote Sensing, vol. 55, no. 4,
715 pp. 1954-1966, doi: 10.1109/TGRS.2016.2631978.
716 Polyakov I., Ashik I., Ivanov V. 2015. IARC Technical Report #9 Report of the NABOS 2015
717 Expedition Activities in the Arctic Ocean,
718 https://nabos.iarc.uaf.edu/NABOS2/data/registered/2015/metadata/Report_2015.pdf.
719 Regan, H. C., Lique, C., Armitage, T. W. K. 2019. The Beaufort Gyre extent, shape, and
720 location between 2003 and 2014 from satellite observations, Journal of Geophysical Research:
721 Oceans, 124, 844– 862. https://doi.org/10.1029/2018JC014379.

722 Reul, N., Grodsky, S.A., Arias, M., Boutin, J. , Catany, R., Chapron, B., D'Amico, F., Dinnat,
723 E., Donlon, C., Fore, A., Fournier, S., Guimbard, S., Hasson, A., Kolodziejczyk, N., Lagerloef,

G., Lee, T., Le Vine, D.M., Lindstrom, E., Maes, C., Mecklenburg, S., Meissner, T., Olmedo, E., Sabia, R., Tenerelli, J., Thouvenin-Masson, C., Turiel, A., Vergely, J.L., Vinogradova, N., Wentz, F., Yueh, S., Sea surface salinity estimates from spaceborne L-band radiometers: An overview of the first decade of observation (2010–2019), Remote Sensing of Environment, Volume 242, 2020, 111769, ISSN 0034-4257, https://doi.org/10.1016/j.rse.2020.111769.

Rodríguez-Fernández, Anterrieu, et al. 2019. SMOS-HR: A high resolution L-band passive radiometer for Earth Science and applications, IEEE Symposium on Geoscience and Remote Sensing 2019, p. 8392-8395

Sakov, P., Counillon, F., Bertino, L., Lisæter, K. A., Oke, P. R., and Korablev, A.: TOPAZ4: an ocean-sea ice data assimilation system for the North Atlantic and Arctic, Ocean Sci., 8, 633–656, https://doi.org/10.5194/os-8-633-2012, 2012.

Shiklomanov, I. A., et al. 1998. World Water Resources. A new appraisal and assessment for the 21ST century. United Nations, Educational, Scientific and Cultural Organization.

Simonsen, M. et al. 2018. CMEMS PRODUCT USER MANUAL For Arctic Ocean Physical and Bio Analysis and Forecasting Products. Copernicus Marine Environment Monitoring Service.

Stroh, J. N., Panteleev, G., Kirillov, S., Makhotin, M., Shakhova, N. 2015. Sea-surface temperature and salinity product comparison against external in situ data in the Arctic Ocean, J. Geophys. Res. Oceans, 120, 7223– 7236, doi:10.1002/2015JC011005.

Tang, W., Yueh, S., Yang, D., Fore, A., Hayashi, A., Lee, T., Fournier, S., Holt, B. 2018. The Potential and Challenges of Using Soil Moisture Active Passive (SMAP) Sea Surface Salinity to Monitor Arctic Ocean Freshwater Changes, Remote Sensing,10.3390/rs10060869.

Tarasenko, A., Supply, A., Kusse-Tiuz, N., Ivanov, V., Makhotin, M., Tournadre, J., Chapron, B., Boutin, J., and Kolodziejczyk, N.: Surface waters properties in the Laptev and the East-

748 Siberian Seas in summer 2018 from in situ and satellite data, Ocean Sci. Discuss.,
749 https://doi.org/10.5194/os-2019-60, in review, 2019.
750 Ulaby, F., Moore, R., Fung, A. 1990. Microwave Remote Sensing: Active and Passive, vol.3,
751 Artech House, Boston, Mass.
752 Vinogradova, N., Lee, T., Boutin, J., Drushka, K., Fournier, S., Sabia, R., Stammer, D., Bayler,
753 E., Reul, N., Gordon, A., Melnichenko, O., Li, L., Hackert, E., Martin, M., Kolodziejczyk, N.,
754 Hasson, A., Brown, S., Misra, S., Lindstrom, E. 2019. Satellite Salinity Observing System:
755 Recent Discoveries and the Way Forward. Front. Mar. Sci. 6: 243. Doi:
756 10.3389/fmars.2019.00243.
757 Waldteufel, P., Vergely, J. L., Cot, C., "A modified cardioid model for processing multiangular
758 radiometric observations," IEEE Transactions on Geoscience and Remote Sensing, vol. 42, pp.
759 1059-1063, 2004.
760 Yueh, S.H., West, R., Wilson, W. J., Li, F. K., Njoku, E. G., Rahmat- Samii, Y. 2001. Error
761 sources and feasibility for microwave remote sensing of ocean surface salinity. IEEE
762 Transactions on Geoscience and Remote Sensing, vol. 39, no. 5, pp. 1049-1060.

763 Xie, J., Raj, R. P., Bertino, L., Samuelsen, A., Wakamatsu, T. 2019. Evaluation of Arctic Ocean
764 surface salinities from the Soil Moisture and Ocean Salinity (SMOS) mission against a regional
765 reanalysis and in situ data, Ocean Science, 15, 5, 1191--1206, https://www.ocean-
766 sci.net/15/1191/2019/, 10.5194/os-15-1191-2019.

767

768 Appendix-A: Acard retrieval in the SMOS level 2 processor

769 As shown by Waldteufel et al. (2004), simultaneous retrieval of the real, e', and imaginary part,
770 e", of dielectric constant from SMOS TB is an ill posed problem as the cost function, rather
771 than a single minimum, exhibits a minimum valley, that can be represented analytically using
772 a modified cardioid model. After carrying out the following change of variable:

$$e' = Acard\,(1 + \cos(Ucard))\cos(Ucard) + Bcard \quad [A1]$$

$$e'' = Acard\,(1 + \cos(Ucard))\sin(Ucard)$$

which is equivalent to:

$$Acard = mcard^{2} / (mcard + e' - Bcard) \quad [A2]$$

$$Ucard = \tan^{-1}(e''/(e'-Bcard))$$

$$\text{with: } mcard = ((e'-Bcard)^2 + e''^2)^{1/2}$$

Bcard corresponds to the observed offset between the observed modified cardioid and the true analytical formulation for a cardioid model. With Bcard = 0.8 (optimal value that minimizes the retrieval error on Acard), it is possible to retrieve the parameter Acard with good accuracy: a minimum of χ^2 is seen as a vertical line corresponding to a constant value of Acard and various values of Ucard. Local minima of χ^2 are also observed for unrealistic negative values of Acard; as it will be described in the following, retrieval of such negative values are avoided by taking an error on prior Acard over the ocean of 20 units or by initiating the retrieval with low Acard value as low card are much better constrained.

It is clear that the minimization of χ^2 parameter does not allow to retrieve a single pair of (e', e'') while it allows to retrieve a single value of Acard, Ucard remaining undetermined.

We found that initiating the retrieval with low Acard prior value ($Acard^{prior}$ =1) and large error on Acard (s_{A_card}=50) allows to avoid retrieval of negative Acard values while avoiding biases on low Acard values and gives the same result over ocean pixels as taking $Acard^{prior}$ deduced from mean SSS and SST.

The ESA L2 Ocean Salinity processor retrieves Acard from SMOS Tb corrected from the roughness model plus atmospheric and galactic noise corrections.

Appendix-B: HEINCKE and POLARSTERN cruise track datasets used in this study

HEINCKE cruise track HE493	https://doi.pangaea.de/10.1594/PANGAEA.887938
HEINCKE cruise track HE387	https://doi.pangaea.de/10.1594/PANGAEA.859752
HEINCKE cruise track HE492	https://doi.pangaea.de/10.1594/PANGAEA.887937
HEINCKE cruise track HE333	https://doi.pangaea.de/10.1594/PANGAEA.859705
HEINCKE cruise track HE451-1	https://doi.pangaea.de/10.1594/PANGAEA.863418
HEINCKE cruise track HE449	https://doi.pangaea.de/10.1594/PANGAEA.863416
HEINCKE cruise track HE408	https://doi.pangaea.de/10.1594/PANGAEA.859774
HEINCKE cruise track HE450	https://doi.pangaea.de/10.1594/PANGAEA.863417
POLARSTERN cruise track ARK-XXVI/2	https://doi.pangaea.de/10.1594/PANGAEA.770035
POLARSTERN cruise track PS109	https://doi.pangaea.de/10.1594/PANGAEA.889548
POLARSTERN cruise track PS93.2	https://doi.pangaea.de/10.1594/PANGAEA.863229
POLARSTERN cruise track ARK-XXVII/1	https://doi.pangaea.de/10.1594/PANGAEA.802811
POLARSTERN cruise track PS99.1	https://doi.pangaea.de/10.1594/PANGAEA.873156
POLARSTERN cruise track PS92	https://doi.pangaea.de/10.1594/PANGAEA.863234
POLARSTERN cruise track ARK-XXVII/3	https://doi.pangaea.de/10.1594/PANGAEA.808835
POLARSTERN cruise track ARK-XXVI/1	https://doi.pangaea.de/10.1594/PANGAEA.770034

POLARSTERN cruise track ARK-XXVI/3	https://doi.pangaea.de/10.1594/PANGAEA.770828
POLARSTERN cruise track ARK-XXVII/2	https://doi.pangaea.de/10.1594/PANGAEA.802812
POLARSTERN cruise track PS107	https://doi.pangaea.de/10.1594/PANGAEA.889535
POLARSTERN cruise track PS100	https://doi.pangaea.de/10.1594/PANGAEA.873158
POLARSTERN cruise track PS93.1	https://doi.pangaea.de/10.1594/PANGAEA.863228
POLARSTERN cruise track PS101	https://doi.pangaea.de/10.1594/PANGAEA.873145
POLARSTERN cruise track PS99.2	https://doi.pangaea.de/10.1594/PANGAEA.873153
POLARSTERN cruise track PS86	https://doi.pangaea.de/10.1594/PANGAEA.858880

Appendix-C: difference of repartition of in-situ measurements used in this study between 1-m and 3-m and between 1-m and 5-m.

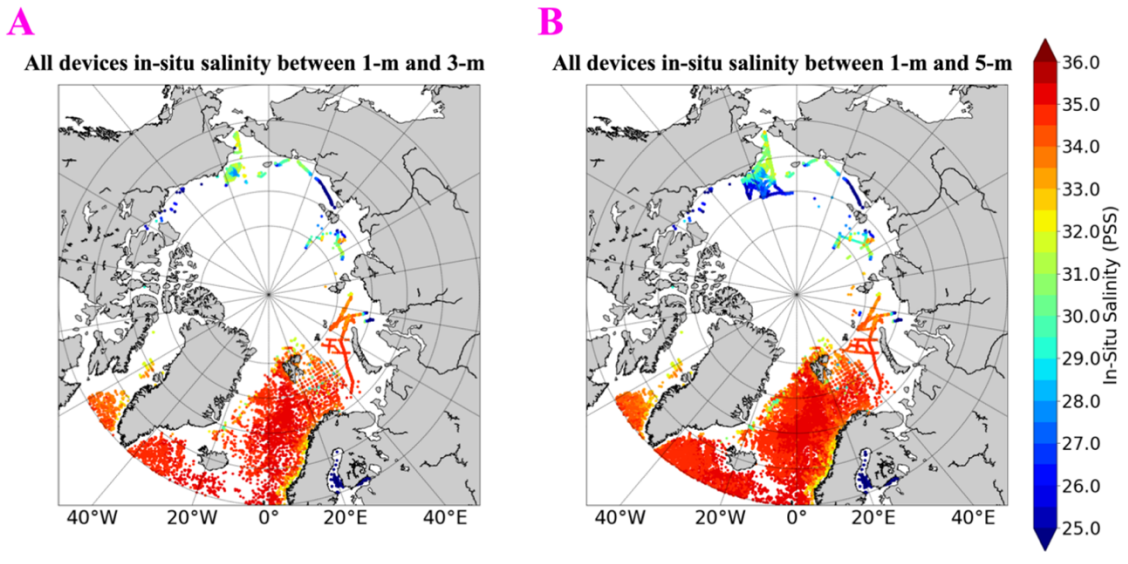

Figure C1: SSS of in-situ measurements used in the study (A) between 1-m and 3-m depth; (B) between 1-m and 5-m depth.

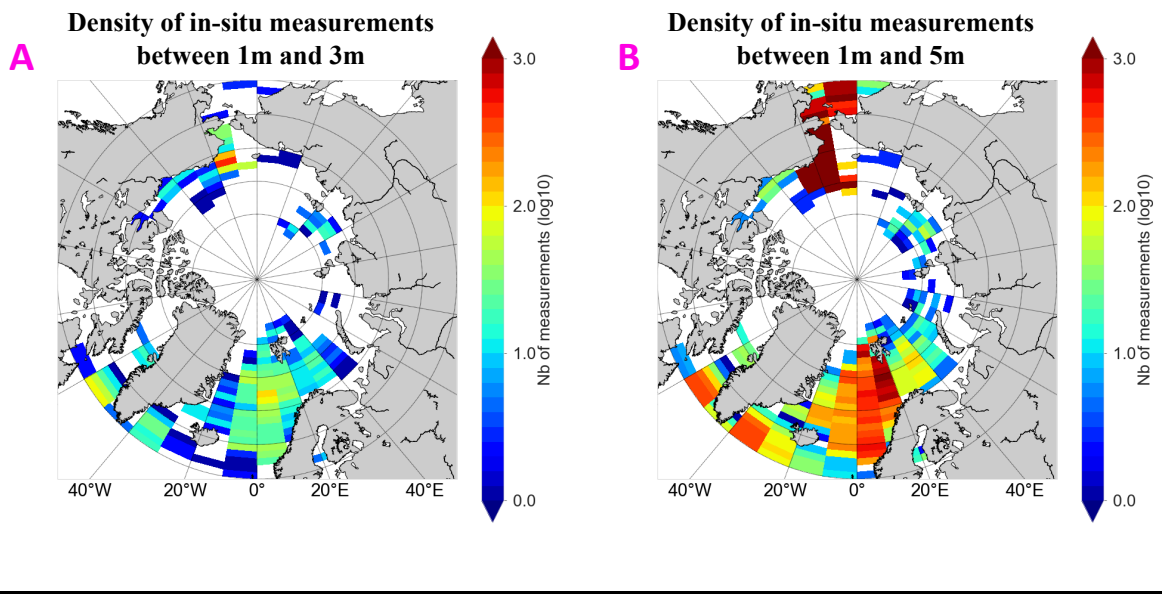

Figure C2: Density of in-situ measurements used in the study (A) between 1-m and 3-m depth; (B) between 1-m and 5-m depth.

Appendix-D: example of differences recorded between SST from OSTIA and SST_{REMSS}.

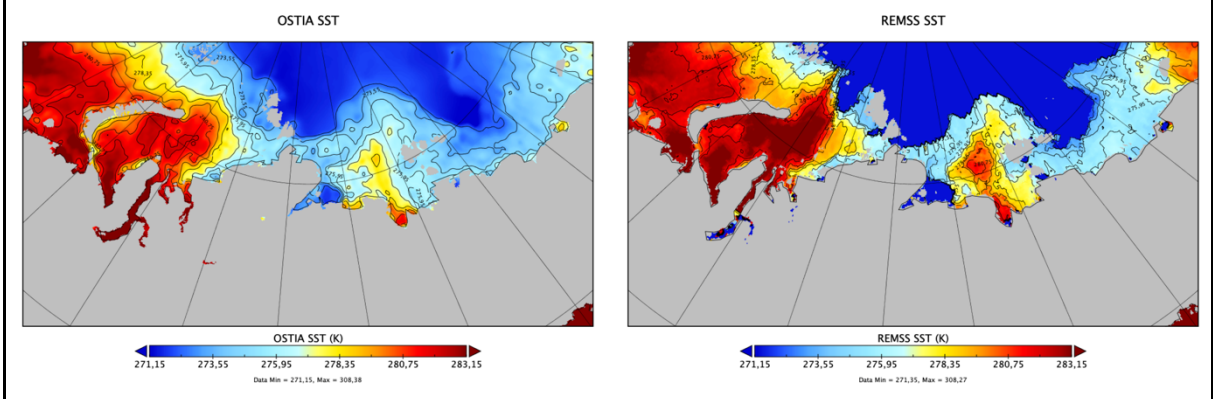

Figure D1: Analyzed SST for 2015/08/15 from (Left) OSTIA; (Right) REMSS (MW +IR)

Appendix-E: MoD, STDD and r between different versions of SMOS SSS and $S_{in\text{-}situ}$ for the different study areas. The number of collocations is equivalent to the table 1.

Cases study	Statistic indicator	SSS_{SMOS}	$SSS_{SMOS\ A}$	$SSS_{SMOS\ T}$	$SSS_{SMOS\ A+T}$
Beaufort Sea	MoD (pss)	-2.12	-1.44	-1.51	-0.83
	STDD (pss)	0.96	0.98	1.08	0.88
	r	0.86	0.83	0.83	0.88
Chukchi Sea	MoD (pss)	-1.50	-1.28	-0.49	-0.28
	STDD (pss)	1.47	1.60	1.18	1.23
	r	0.84	0.81	0.89	0.86
Laptev Sea	MoD (pss)	-1.97	-1.39	-0.43	0.12
	STDD (pss)	1.82	2.16	1.07	1.17
	r	0.53	0.40	0.80	0.75
Barents Sea	MoD (pss)	-1.59	-0.24	-1.49	-0.17
	STDD (pss)	0.96	0.97	0.94	0.94
	r	-0.03	-0.02	-0.05	-0.02
Atlantic Area	MoD (pss)	-1.29	-0.55	-1.25	-0.51
	STDD (pss)	1.02	1.15	1.00	1.13
	r	0.01	-0.05	0.02	-0.05
Arctic Ocean	MoD (pss)	-1.54	-0.77	-0.99	-0.27

	STDD (pss)	1.46	1.60	1.32	1.28
	r	0.92	0.92	0.93	0.94

801

802 Appendix-F: MoD, STDD, r and N (number of collocations) between different versions of
803 SMOS SSS or TOPAZ SSS and in-situ measurements for the different study areas (with
804 $SSS_{SMOS\ A+T}$ derived using SST_{REMSS} in black and $SSS_{SMOS\ A+T}$ derived using $SST_{REMSS\ MWO}$ in
805 bold black – collocations are not exactly the same due to a difference of sea ice mask between
806 SST_{REMSS} and $SST_{REMSS\ MWO}$, and a difference of coverage close from coast – colocations with
807 in-situ measurements are the same between SSS_{SMOS}, $SSS_{SMOS\ A+T}$ and SSS_{TOPAZ}).

Cases study	Statistic indicator	SSS_{SMOS}	$SSS_{SMOS\ A+T}$	SSS_{TOPAZ}
Beaufort Sea	MoD (pss)	-2.25 **-2.25**	-0.98 **-0.96**	3.99 **3.99**
	STDD (pss)	0.94 **0.94**	0.83 **0.87**	1.07 **1.07**
	r	0.81 **0.81**	0.84 **0.84**	0.81 **0.81**
	N	3128 **3128**	3128 **3128**	3128 **3128**
Chukchi Sea	MoD (pss)	-1.39 **-1.39**	-0.21 **-0.27**	1.94 **1.94**
	STDD (pss)	1.30	1.08	1.79

		1.30	**1.07**	**1.79**
	r	0.86 **0.86**	0.91 **0.90**	0.87 **0.87**
	N	86917 **86917**	86917 **86917**	86917 **86917**
Laptev Sea	MoD (pss)	-2.45 **-2.45**	-0.17 **-0.19**	0.82 **0.82**
	STDD (pss)	1.69 **1.69**	1.03 **1.01**	1.46 **1.46**
	r	0.61 **0.61**	0.74 **0.75**	0.32 **0.32**
	N	3190 **3190**	3190 **3190**	3190 **3190**
Barents Sea	MoD (pss)	-1.58 **-1.58**	-0.16 **-0.15**	-0.20 **-0.20**
	STDD (pss)	0.95 **0.95**	0.93 **0.93**	0.49 **0.49**
	r	-0.07 **-0.07**	-0.05 **-0.05**	0.19 **0.19**
	N	10762	10762	10762

		10762	**10762**	**10762**
Atlantic area	MoD (pss)	-1.28 **-1.28**	-0.50 **-0.49**	0.01 **0.01**
	STDD (pss)	0.99 **0.99**	1.10 **1.09**	0.10 **0.10**
	r	0.02 **0.02**	-0.04 **-0.04**	0.70 **0.70**
	N	2865 **2865**	2865 **2865**	2865 **2865**
Arctic Ocean	MoD (pss)	-1.46 **-1.46**	-0.21 **-0.25**	1.20 **1.20**
	STDD (pss)	1.31 **1.31**	1.15 **1.15**	1.86 **1.86**
	r	0.93 **0.93**	0.95 **0.95**	0.89 **0.89**
	N	148655 **148655**	148655 **148655**	148655 **148655**

Appendix-G: example of differences recorded between $SSS_{SMOS\ A+T}$ using SST_{REMSS} or using $SST_{REMSS\ MWO}$ in comparison of differences between SSS_{SMOS} and $SSS_{SMOS\ A+T}$ (using SST_{REMSS}).

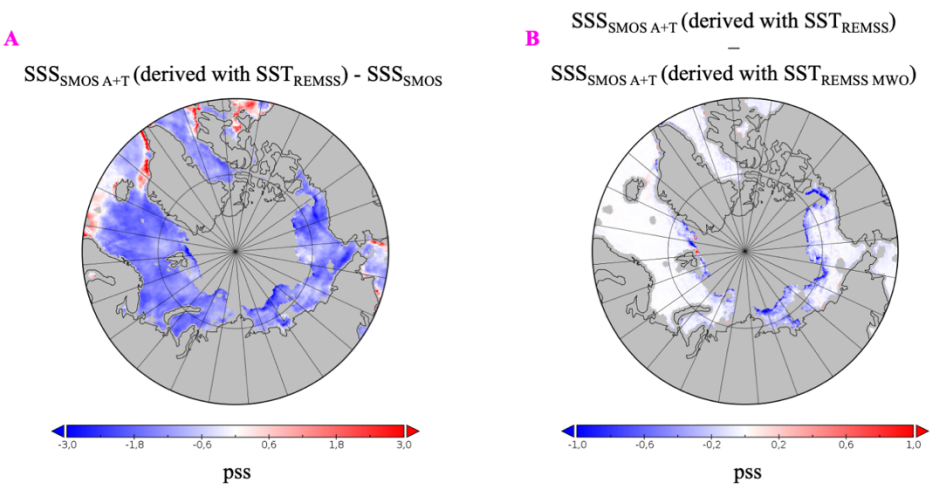

Figure G1: (A) difference between SSS_{SMOS} and $SSS_{SMOS\ A+T}$ (computed using SST_{REMSS}) average for the period from August to October 2017; (B) difference between $SSS_{SMOS\ A+T}$ (computed using SST_{REMSS}) and $SSS_{SMOS\ A+T}$ (computed using $SST_{REMSS\ MWO}$) average for the period from August to October 2017.

Appendix-H: MoD, STDD, r and N (number of collocations) between different versions of SMOS SSS or TOPAZ SSS and in-situ measurements for the different study areas. In black, new SMOS SSS, in blue SMOS BEC v2 (Olmedo et al. 2018) and in red SMOS CEC v3 (Boutin et al. 2018).

Cases study	Statistic indicator	SSS_{SMOS}	$SSS_{SMOS\ A+T}$	SSS_{TOPAZ}
Beaufort Sea	MoD (pss)	-2.12 (1.04) (3.51)	-0.83	3.67
	STDD (pss)	0.96 (1.85) (2.35)	0.88	1.18

	r	0.86 (0.78) (0.76)	0.88	0.86
	N	(3912) (3976) (4434)	3912	3912
Chukchi Sea	MoD (pss)	-1.50 (0.53) (3.00)	-1.28	1.97
	STDD (pss)	1.47 (1.48) (1.87)	1.23	1.78
	r	0.84 (0.83) (0.54)	0.88	0.86
	N	(90721) (100908) (105986)	90721	90721
Laptev Sea	MoD (pss)	-1.97 (0.37) (0.59)	0.11	1.51
	STDD (pss)	1.82	1.17	1.89

		(1.85) (2.35)		
	r	0.53 (0.39) (-0.10)	0.75	0.04
	N	(4048) (3391) (3391)	4048	4048
Barents Sea	MoD (pss)	-1.59 (-0.01) (0.35)	-0.17	-0.19
	STDD (pss)	0.96 (0.88) (1.39)	0.94	0.50
	N	(10879) (15571) (18622)	10879	10879
	r	-0.03 (0.31) (-0.14)	-0.04	0.19
Atlantic Area	MoD (pss)	-1.29 (0.01)	-0.51	0.01

		(0.01)		
	STDD (pss)	1.02 (0.27) (0.66)	1.13	0.10
	r	0.01 (0.38) (-0.05)	-0.05	0.70
	N	(2876) (5863) (6168)	2876	2876
Arctic Ocean	MoD (pss)	-1.54 (0.12) (1.55)	-0.27	1.25
	STDD (pss)	1.46 (1.65) (2.30)	1.28	1.86
	r	0.92 (0.93) (0.86)	0.94	0.89
	N	(156986) (196665) (225904)	156986	156986

817

818
819